drones

MDPI

Article

Cooperative Pursuit of a Faster Evader by Underactuated USVs in Obstacle Environments: A Neighboring Time-Compensation Approach

Ziqi Cao *, Zhenghua Liu and Weihong Wang

School of Automation Science and Electrical Engineering, Beihang University, Beijing 100191, China; lzh@buaa.edu.cn (Z.L.); wwh2005@buaa.edu.cn (W.W.)
* Correspondence: caozq@buaa.edu.cn

Highlights

What are the main findings?

- A signed path-connection margin quantifies neighboring time compensation and provides a proven sufficient condition for collective geometric arrival advantage along a collision-free connecting path.
- A hierarchical framework optimizes nominal trajectories using the proposed margin and realizes them through surge–yaw tracking, enabling underactuated USVs to capture a faster evader in simulation.

What is the implication of the main finding?

- The margin provides future studies with a quantitative criterion for evaluating and optimizing neighboring cooperation in obstacle environments.
- The results highlight the potential of coordinated USV teams to compensate for individual speed disadvantages in maritime interception.

Abstract

This paper investigates the cooperative pursuit of a faster evader by multiple underactuated unmanned surface vehicles (USVs) in obstacle environments. Unequal detours alter the relative arrival advantages of the pursuing and evading vehicles, while underactuation and disturbances complicate the execution of cooperative motion. Firstly, a neighboring time-compensation criterion is developed using geometric travel-time indices at selected Cartesian-oval points, accounting for a nonzero capture radius. A signed path-connection margin yields a sufficient condition under which at least one of two neighboring pursuers has a geometric arrival advantage at each point along a connecting path. Secondly, a distributed receding-horizon planner optimizes surge and yaw acceleration sequences through particle swarm optimization (PSO). Control barrier function (CBF) projection precedes reference propagation, allowing terminal cooperation to be evaluated after safety corrections with obstacle-avoidance and velocity constraints imposed on the reference trajectories. Thirdly, a coordinated surge–yaw controller constructs virtual commands from position errors and measured sway motion, with extended state observers providing disturbance compensation. The input-to-state stability of the tracking errors is established with respect to observation residuals and control-input deviations. Finally, a simulation involving 5 USVs and 24 circular obstacles demonstrates capture of the faster evader with positive obstacle clearance and small position-tracking errors under time-varying disturbances.

Check for updates

Academic Editor: Bing Huang

Received: 21 October 2026
Revised: 19 November 2026
Accepted: 23 November 2026
Published: 26 November 2026

Copyright: © 2026 by the authors. Licensee MDPI, Basel, Switzerland. This article is an open access article distributed under the terms and conditions of the Creative Commons Attribution (CC BY) license.

Keywords: cooperative pursuit; underactuated unmanned surface vehicles; neighboring time compensation; control barrier functions; Cartesian ovals

1. Introduction

Unmanned surface vehicles (USVs) provide an autonomous platform for maritime surveillance and environmental monitoring [1]. Cooperative pursuit supports target interception and containment in maritime security missions. When an evader moves faster than each individual pursuer, the pursuit team must coordinate its approach while limiting escape opportunities between neighboring vessels. Obstacles complicate this coordination by imposing different detours on the pursuers and evader. Moreover, underactuated USVs must realize the planned motion through surge force and yaw moment while experiencing sway motion and environmental disturbances. These requirements motivate the joint consideration of cooperative pursuit planning and position tracking.

The geometry of cooperative pursuit of a faster evader by multiple slower pursuers has been extensively studied [2]. Earlier analyses related capture conditions to the speed ratio, initial configuration, and intersections of neighboring Apollonius circles [3]. Ramana and Kothari developed a cooperative strategy based on overlapping Apollonius circles [4], while Fang et al. designed a distributed strategy that balances encirclement formation with approach to the evader [5]. Fishing-game analyses connect capture and escape to neighboring pursuer geometry [6,7], motivating the coordination of angular regulation and target approach [8]. With a nonzero capture radius, a pursuer only needs to reach the capture disk around a prospective evader location. Garcia and Bopardikar characterized the resulting equal-time geometry using Cartesian ovals (COs) [9], and Zhou et al. investigated CO-based containment with heterogeneous pursuers [10]. COs therefore provide a basis for comparing geometric arrival advantages and describing collective angular coverage.

Obstacles affect both motion safety and the relative arrival advantages of the pursuers and the evader. The Apollonius-circle and CO constructions described above compare straight-line travel times. Unequal obstacle-induced detours can change this ordering, so coverage inferred from obstacle-free geometry may overestimate the pursuers' arrival advantage and overlook potential escape corridors. Shortest-path methods for curved obstacles provide a means of accounting for these detours [11,12]. Cooperative pursuit with collision avoidance has also been investigated. For example, Zhou et al. combined artificial potential fields with virtual target points for slower pursuit vehicles operating among obstacles [13]. However, ensuring collision-free motion does not by itself establish how obstacles alter the relative arrival advantages of neighboring pursuers and the evader. This motivates explicitly incorporating obstacle-dependent travel-time comparisons into the coordination of neighboring pursuers.

Control barrier functions (CBFs) incorporate safety constraints into feedback control through inequalities on the control input [14]. Exponential CBFs [15] and high-order control barrier functions (HOCBFs) [16,17] extend this construction to constraints for which the input appears after repeated differentiation. Applications include obstacle avoidance with limited actuation [18], distributed safe navigation [19], and collision avoidance in pursuit–evasion scenarios [20]. Safety filtering has also been incorporated into sampling-based predictive control to evaluate candidate motion after control correction [21]. For cooperative pursuit, such corrections can change subsequent access to neighboring interception regions. Candidate controls should therefore be evaluated using the trajectories generated after safety filtering.

Related USV studies address the connection between cooperative motion and underactuated control. Peng et al. [22] reviewed trajectory-guided, path-guided, and target-guided coordination of multiple autonomous surface vehicles and associated collision-avoidance challenges, while Ning et al. [23] combined observer-based distributed guidance with neuro-adaptive control for formation tracking of underactuated USVs under input quantization. Feng et al. developed an event-triggered framework for simultaneous trajectory tracking and stabilization of underactuated USVs [24]. Zhu et al. used distributed nonlinear model predictive control for multi-target tracking and surrounding under unknown disturbances [25]. Jiang et al. combined finite-time fuzzy prediction with input-to-state safe HOCBFs for cooperative target enclosing among obstacles [26]. Li et al. investigated pursuit of a partially unknown faster evader by combining Apollonius-circle-based planning, safety optimization, and dynamic control based on extended state observers (ESOs) [27]. However, their angular coverage criterion incorporates neither the capture radius specified in the pursuit objective nor obstacle-dependent travel times. In particular, neglecting unequal detours may overestimate the pursuers' arrival advantage, potentially allowing the evader to exploit unrecognized escape routes in complex obstacle environments. For known circular obstacles, the present work combines existing CO geometry with collision-free path-length comparisons and establishes a signed connection margin that provides a sufficient condition for pairwise geometric arrival advantage along a connecting path.

Motivated by these observations, this paper develops a hierarchical cooperative pursuit method for multiple slower underactuated USVs pursuing a faster evader among known, disjoint circular obstacles, with capture defined by a finite separation threshold. Each pursuer selects evaluation points on the gap-facing sides of its two neighboring COs. Collision-free shortest-path lengths define geometric travel-time indices and signed path-connection margins, combining the pursuer's own geometric advantage with its neighbor's time lead or delay. These margins form a terminal objective for distributed receding-horizon planning with particle swarm optimization (PSO) [28] and CBF filtering, termed RH–PSO–CBF. A CBF quadratic program filters candidate surge and yaw accelerations before reference propagation. The lower layer tracks the resulting position trajectory through coordinated surge–yaw control with ESO disturbance compensation.

The main contributions are as follows:

1. A CO-based neighboring time-compensation criterion is established to quantify how obstacle-induced detours alter the relative arrival advantages of the pursuit team. A signed path-connection margin characterizes both the neighbor's arrival lead and delay. A sufficient condition is proved under which at least one of the two pursuers has a geometric arrival advantage at every point along a connecting path, providing a quantitative criterion for cooperation in obstacle environments.
2. A distributed RH–PSO–CBF strategy is developed to anticipate the effect of obstacle-avoidance maneuvers on neighboring cooperation. Each pursuer optimizes surge and yaw acceleration sequences according to the predicted terminal connection margins on both angular sides. The objective is evaluated on CBF-filtered trajectories, allowing pursuit decisions to account for the changes in arrival advantages caused by safety corrections with obstacle-avoidance and velocity constraints imposed on the reference trajectories.
3. A coordinated surge–yaw tracking law is derived for underactuated USVs, with virtual commands determined by position errors and measured sway motion. The control design cancels the nominal coupling terms in the Lyapunov derivative and establishes input-to-state stability of the tracking errors with respect to ESO estimation residuals and deviations from the ideal control inputs.

The remainder of the paper is organized as follows. Section 2 presents the USV model, problem formulation, and CO geometry. Section 3 develops neighboring time compensation, distributed RH–PSO–CBF planning, and coordinated surge–yaw tracking control. Section 4 presents the simulation setup and analyzes the pursuit, obstacle avoidance, and tracking results. Section 5 concludes the paper.

2. Problem Formulation and Cartesian-Oval Geometry

2.1. Motion Model and Problem Setup

Consider $N \geq 3$ underactuated unmanned surface vehicles (USVs), denoted by P_i, $i = 1, \ldots, N$, pursuing a moving surface target E. The USVs operate in a horizontal plane, with heave, roll, and pitch neglected. For pursuer P_i, let $p_i = [x_i, y_i]^\top \in \mathbb{R}^2$ denote its position in the inertial frame and ψ_i its yaw angle. The body-frame velocity vector is $\nu_i = [u_i, v_i, r_i]^\top$, where u_i, v_i, and r_i denote the surge velocity, sway velocity, and yaw rate, respectively. Define

$$R(\psi) = \begin{bmatrix} \cos\psi & -\sin\psi \\ \sin\psi & \cos\psi \end{bmatrix}. \tag{1}$$

The planar kinematics are

$$\dot{p}_i = R(\psi_i) \begin{bmatrix} u_i \\ v_i \end{bmatrix}, \qquad \dot{\psi}_i = r_i. \tag{2}$$

Hence, $\|\dot{p}_i\| = \sqrt{u_i^2 + v_i^2}$.

Following the three-degree-of-freedom marine-craft formulation [29], a diagonal nominal inertia matrix and linear nominal damping are adopted. The dynamics of the USV pursuers are written as

$$\begin{aligned} \dot{u}_i &= \frac{m_v}{m_u} v_i r_i - \frac{d_u}{m_u} u_i + \frac{\tau_{u,i}}{m_u} + w_{u,i}, \\ \dot{v}_i &= -\frac{m_u}{m_v} u_i r_i - \frac{d_v}{m_v} v_i + w_{v,i}, \\ \dot{r}_i &= \frac{m_u - m_v}{m_r} u_i v_i - \frac{d_r}{m_r} r_i + \frac{\tau_{r,i}}{m_r} + w_{r,i}. \end{aligned} \tag{3}$$

Here, $m_u, m_v, m_r > 0$ are effective inertia coefficients, and $d_u, d_v, d_r > 0$ are nominal damping coefficients. The control inputs $\tau_{u,i}$ and $\tau_{r,i}$ are the surge force and yaw moment. The unknown terms $w_{u,i}, w_{v,i}, w_{r,i}$ represent residual modeling uncertainties and external disturbances in acceleration units. For subsequent design, define $a_v = d_v/m_v$ and $b_v = m_u/m_v$, so that $\dot{v}_i = -a_v v_i - b_v u_i r_i + w_{v,i}$.

Assumption 1. *For each pursuer P_i, the unknown terms $w_{j,i}$, $j \in \{u, v, r\}$ are differentiable and satisfy $|w_{j,i}(t)| \leq W_j$, $|\dot{w}_{j,i}(t)| \leq D_j$, where W_j and D_j are known nonnegative constants.*

The actuator inputs satisfy $\tau_{j,\min} \leq \tau_{j,i} \leq \tau_{j,\max}$, $j \in \{u, r\}$. The study considers forward operation subject to $0 < \underline{U} \leq u_i \leq \overline{U}$, $|r_i| \leq \overline{R}$, and $u_i^2 + v_i^2 \leq V_p^2$, where $\underline{U}$, $\overline{U}$, and $\overline{R}$ are prescribed positive constants, and V_p is the speed limit of the pursuers. The pursuers may vary their speeds within these constraints.

The evader is represented by its position $p_e \in \mathbb{R}^2$ and velocity heading ψ_e. Its motion satisfies

$$\dot{p}_e = V_e q(\psi_e), \qquad \dot{\psi}_e = \frac{a_e}{V_e}, \qquad |a_e| \leq \bar{a}_e, \tag{4}$$

where $q(\psi) = [\cos\psi, \sin\psi]^\top$, $V_e > 0$ is constant, and a_e is the signed normal acceleration. The speed advantage of the evader is specified by

$$0 < V_p < V_e, \qquad \lambda = \frac{V_p}{V_e} \in (0,1). \tag{5}$$

Define the relative position and distance by

$$\boldsymbol{\rho}_i = p_i - p_e, \qquad d_i = \|\boldsymbol{\rho}_i\|. \tag{6}$$

Given a capture radius $d_c > 0$, capture occurs when

$$\min_{i=1,\dots,N} d_i(t) \le d_c. \tag{7}$$

The pursuit terminates at the first time that (7) holds. Consequently, $d_i(t) > d_c$ for every pursuer before capture.

Assumption 2. *The environment contains M known, static circular obstacles with centres $o_m \in \mathbb{R}^2$ and radii $R_m > 0$, $m = 1, \dots, M$. The radii include the clearance required by the vessel dimensions, and the resulting disks are pairwise disjoint:*

$$\|o_m - o_n\| > R_m + R_n, \qquad m \neq n. \tag{8}$$

The free space for vehicle centres is

$$\mathcal{F} = \Big\{ p \in \mathbb{R}^2 : \|p - o_m\| \ge R_m, \quad m = 1, \dots, M \Big\}. \tag{9}$$

Initially, $p_i(0), p_e(0) \in \mathcal{F}$ and $d_i(0) > d_c$ for all i. Both the pursuers and the evader are required to remain in $\mathcal{F}$.

The objective is to design a distributed cooperative pursuit strategy that achieves Equation (7) while respecting the dynamics, actuator limits, motion constraints, and obstacle constraints. The evader seeks to avoid capture subject to its own motion and obstacle constraints.

2.2. Cartesian Ovals and Neighbor Geometry

To describe the pursuit geometry with a nonzero capture radius, consider an arbitrary point $S \in \mathbb{R}^2$. Obstacles and turning constraints are temporarily disregarded in this geometric comparison. The straight-line travel times are

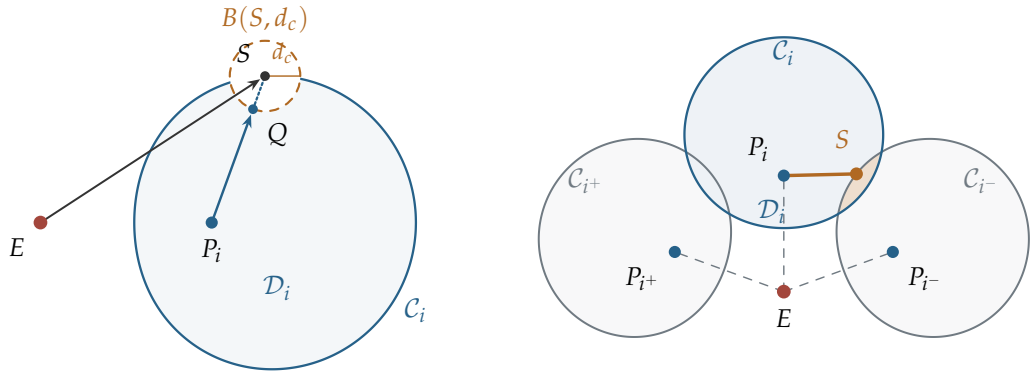
$$T_i^0(S) = \frac{[\|p_i - S\| - d_c]_+}{V_p}, \qquad T_e^0(S) = \frac{\|p_e - S\|}{V_e}, \tag{10}$$

where $[z]_+ = \max\{z, 0\}$. The pursuer's time is measured to the capture disk $B(S, d_c) = \{y \in \mathbb{R}^2 : \|y - S\| \le d_c\}$, whereas the evader's time is measured to S.

Definition 1. *The Cartesian oval (CO) associated with the pursuer P_i and the evader E is the locus of points satisfying $T_i^0(S) = T_e^0(S)$ [9]. Before capture, $d_i > d_c$, and this locus is given by*

$$\mathcal{C}_i = \Big\{ S \in \mathbb{R}^2 : \|p_i - S\| - \lambda\|p_e - S\| - d_c = 0 \Big\}. \tag{11}$$

For $S \in \mathcal{C}_i$, let Q be the first intersection of the segment $p_i S$ with the boundary of $B(S, d_c)$, as shown in Figure 1a.



(**a**) Equal-time geometry (**b**) Neighbors and cooperative coverage

Figure 1. Cartesian-oval geometry and cooperative coverage. (**a**) For $S \in \mathcal{C}_i$, the pursuer reaches Q on the capture-disk boundary when the evader reaches S in the straight-line comparison. The dotted segment QS is excluded from the pursuer's travel time. (**b**) The clockwise and counterclockwise neighbors of P_i are P_{i^-} and P_{i^+}, respectively. The point $S \in \mathcal{C}_{i^-} \cap \mathcal{D}_i$ illustrates coverage of a neighboring CO boundary point by P_i; the segment p_iS is contained in $\mathcal{D}_i$. The darker shading indicates $\mathcal{D}_i \cap \mathcal{D}_{i^-}$.

The evader reaches S at the same time that the pursuer reaches Q and enters the capture disk. Thus, $\mathcal{C}_i$ is an equal-arrival-time curve in the obstacle-free geometric setting. The closed region enclosed by $\mathcal{C}_i$ is denoted by $\mathcal{D}_i = \{S \in \mathbb{R}^2 : T_i^0(S) \leq T_e^0(S)\}$ and is referred to as the geometric dominance region of P_i. Within this comparison, P_i can reach the capture disk centred at any point in $\mathcal{D}_i$ no later than the evader reaches that point.

Definition 2. *At a given time t, let $\phi_i = \operatorname{atan2}((\boldsymbol{\rho}_i)_y, (\boldsymbol{\rho}_i)_x)$ be the line-of-sight bearing from the evader to P_i. Order the pursuers counterclockwise about the evader according to these bearings. The pursuer immediately preceding P_i in this cyclic order is its clockwise neighbor P_{i^-}, and the pursuer immediately following P_i is its counterclockwise neighbor P_{i^+}. The angular-neighbor set is $\mathcal{N}_i(t) = \{i^-, i^+\}$.*

The following lemma relates coverage at a neighboring CO boundary point to coverage along a connecting segment, as illustrated in Figure 1b.

Lemma 1. *For $j \in \mathcal{N}_i(t)$, let $S \in \mathcal{C}_j \cap \mathcal{D}_i$. Then $[p_i, S] \subseteq \mathcal{D}_i$, i.e.,*

$$T_i^0(X) \leq T_e^0(X), \qquad \forall X \in [p_i, S]. \tag{12}$$

Proof. For any $X \in [p_i, S]$, the triangle inequality gives

$$\begin{aligned} &\|p_i - X\| - \lambda\|p_e - X\| - d_c \\ &\leq \|p_i - S\| - \lambda\|p_e - S\| - d_c \\ &\quad - (1-\lambda)\|S - X\| \leq 0. \end{aligned}$$

Thus, $X \in \mathcal{D}_i$, which proves the claim. □

Obstacles may impose unequal detours on neighboring pursuers and the evader, so the overlap between $\mathcal{D}_i$ and $\mathcal{D}_j$ alone does not determine their geometric arrival-time ordering. The next section develops a cooperative coverage criterion along collision-free paths and uses it to construct a compensation mechanism for obstacle-induced arrival delays.

Remark 1. *The CO geometry above incorporates the capture radius but uses straight-line travel times. Unequal obstacle-induced detours can change the relative arrival advantages, so overlap between neighboring CO dominance regions alone does not determine the corresponding arrival-time ordering along collision-free paths. This motivates the obstacle-dependent travel-time comparisons and neighboring time-compensation criterion in Section 3.1.*

3. Hierarchical Cooperative Pursuit with Neighboring Time Compensation

The hierarchical framework in Figure 2 combines cooperative planning and position tracking. Section 3.1 develops neighboring time compensation through obstacle-avoiding geometric travel-time comparisons. Section 3.2 incorporates the resulting connection margins into distributed receding-horizon PSO–CBF (RH–PSO–CBF) planning to generate reference velocities $u_{d,i}, v_{d,i}, r_{d,i}$ and the corresponding position trajectory $p_{d,i}$. Section 3.3 presents coordinated surge–yaw control for position tracking, with extended-state observers (ESOs) for disturbance compensation. The framework executes the first reference segment and replans using updated measurements.

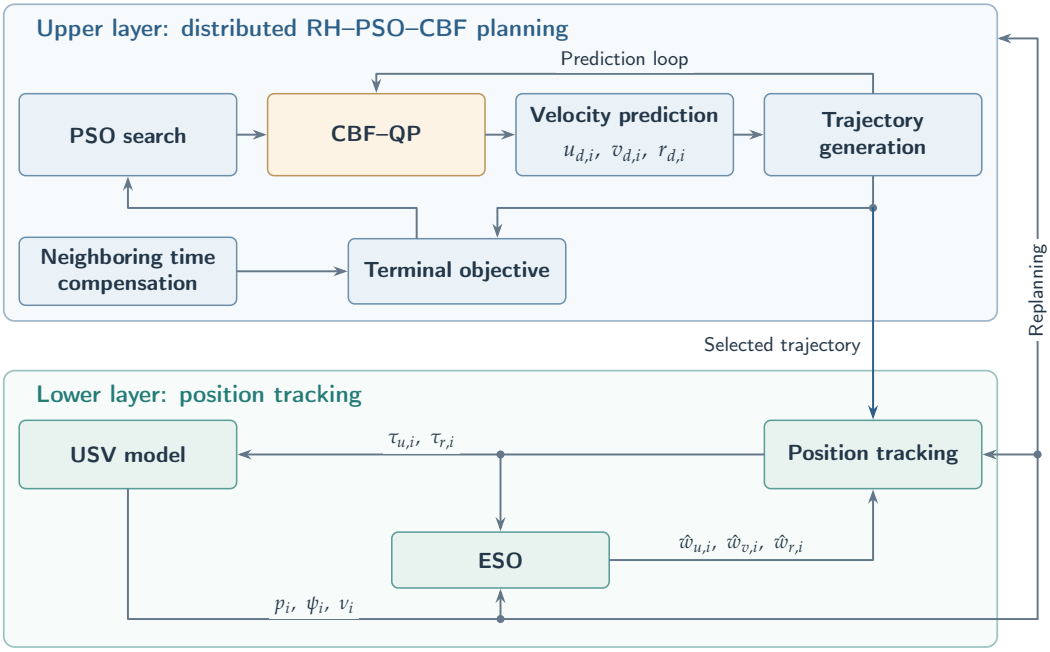


Figure 2. Hierarchical cooperative pursuit framework for pursuer P_i. The upper layer uses RH–PSO–CBF planning to generate the reference trajectory. The lower layer performs position tracking through coordinated surge–yaw control with three-channel ESO disturbance compensation.

3.1. CO-Based Neighboring Time Compensation

3.1.1. Geometric Travel-Time Indices and CO Evaluation Points

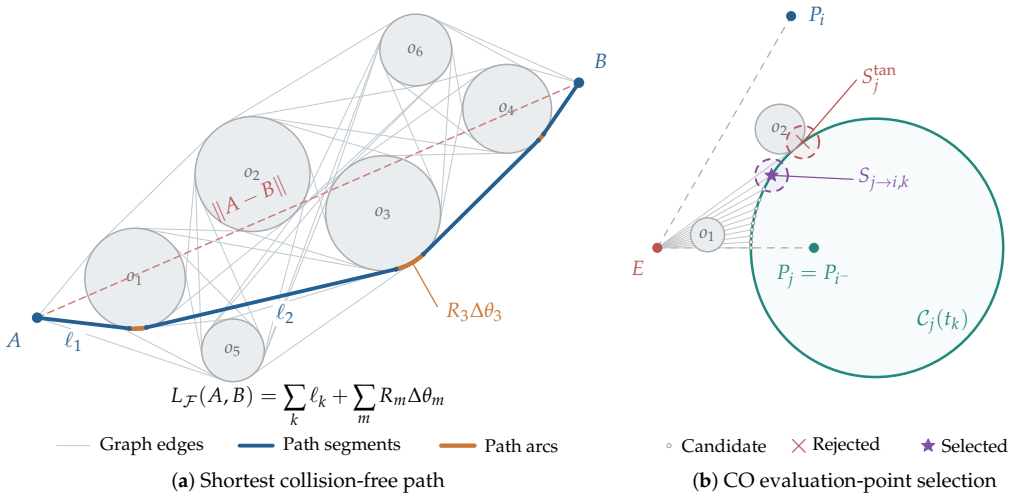
Definition 3. *For $A, B \in \mathcal{F}$, $L_{\mathcal{F}}(A, B)$ denotes the length of a shortest collision-free path from A to B, allowing contact with obstacle boundaries. It is computed by Dijkstra's algorithm on a tangent graph containing collision-free point–circle tangents, inner and outer circle–circle tangents, circular boundary arcs, and the direct segment AB when collision-free, with each edge weighted by its length [12].*

This distance extends the straight-line geometry to $\mathcal{F}$, providing the shortest distance between two points for geometric arrival-time estimation. It satisfies the triangle inequality

and reduces to $\|A - B\|$ when AB is collision-free. Replacing the straight-line distances in Equation (10) yields the geometric travel-time indices, for any $X \in \mathcal{F}$,

$$T_i(X; p_i) = \frac{[L_{\mathcal{F}}(p_i, X) - d_c]_+}{V_p}, \qquad T_e(X; p_e) = \frac{L_{\mathcal{F}}(p_e, X)}{V_e}. \tag{13}$$

When $B(X, d_c) \subseteq \mathcal{F}$, $T_i(X; p_i)$ gives the geometric time for pursuer P_i to reach the capture disk $B(X, d_c)$ at speed V_p, whereas $T_e(X; p_e)$ gives that for the evader to reach X at speed V_e. The tangent graph and the resulting shortest collision-free path from A to B are illustrated in Figure 3a.



(**a**) Shortest collision-free path (**b**) CO evaluation-point selection

Figure 3. Geometric path distance and CO evaluation-point selection. (**a**) A tangent graph and its shortest path for six circular obstacles. Blue segments and orange arcs form the path; the dashed segment AB is obstructed. (**b**) The tangent point is rejected because its capture disk intersects an obstacle; the nearest valid sampled CO point is selected for $j = i^-$.

Remark 2. *The shortest paths in Definition 3 connect straight segments and circular boundary arcs tangentially, avoiding abrupt changes in travel direction at their junctions. The travel-time indices in Equation (13), however, do not explicitly incorporate vehicle-specific turning and acceleration constraints or the full vehicle dynamics. Proposition 1 therefore establishes a sufficient condition for geometric arrival advantage under these indices, without by itself guaranteeing the same arrival-time ordering under the full vehicle dynamics.*

Definition 4. *At each planning instant t_k, an evaluation point $S_{j\to i,k}$ for pursuer P_i and its neighbor $j \in \mathcal{N}_{i,k} = \mathcal{N}_i(t_k)$ is a point on the side of $\mathcal{C}_j(t_k)$ facing their common angular gap and satisfying*

$$S_{j\to i,k} \in \mathcal{C}_j(t_k), \qquad B(S_{j\to i,k}, d_c) \subseteq \mathcal{F}. \tag{14}$$

The counterclockwise side is used for $j = i^-$, and the clockwise side for $j = i^+$. Let $S_j^{\tan}$ be the tangent point from p_e to $\mathcal{C}_j(t_k)$ on the corresponding side. It is selected if it lies within the adjacent angular gap and its capture disk lies entirely in $\mathcal{F}$.

Otherwise, ray directions are sampled uniformly from $p_e p_j$ toward $p_e S_j^{\tan}$, stopping at $p_e p_i$ if encountered first. The first intersection of each ray with $\mathcal{C}_j(t_k)$ gives a candidate. Among candidates whose capture disks lie entirely in $\mathcal{F}$, the one closest to $S_j^{\tan}$ in Euclidean distance is selected, as illustrated in Figure 3b. The selected points remain fixed in world coordinates during the local optimization.

3.1.2. Neighboring Time Compensation and Path Connection

Let $S = S_{j\to i,k}$ be an evaluation point satisfying Definition 4. Since $S \in \mathcal{C}_j(t_k)$, the straight-line travel times satisfy $T_j^0(S) = T_e^0(S)$, whereas obstacle-induced detours may lead to $T_j(S) \neq T_e(S)$. Define the neighbor's time lead by $\beta_j(S) = T_e(S) - T_j(S)$. A positive value indicates a geometric arrival advantage of P_j over the evader at S, and a negative value indicates a delay. Let

$$D_i = L_{\mathcal{F}}(p_e, p_i), \qquad L_i(S) = L_{\mathcal{F}}(p_i, S), \qquad \kappa = V_p^{-1} + V_e^{-1}. \tag{15}$$

Define the own path-length threshold

$$\rho_i^{\text{path}} = \frac{V_p D_i + V_e d_c}{V_p + V_e} \tag{16}$$

and the signed path-connection margin

$$\mu_{ij}(S) = \rho_i^{\text{path}} + \frac{\beta_j(S)}{\kappa} - L_i(S). \tag{17}$$

The following proposition shows that $\mu_{ij}(S) \geq 0$ ensures $\min\{T_i(X), T_j(X)\} \leq T_e(X)$ at every point X on a shortest collision-free path from p_i to S.

Proposition 1. *Before capture, fix a neighbor j and an evaluation point S satisfying $B(S, d_c) \subseteq \mathcal{F}$. Let $\gamma(s)$ denote the point reached after traversing a length s along a shortest collision-free path from p_i to S, where $0 \leq s \leq L_i(S)$. If $\mu_{ij}(S) \geq 0$, then*

$$\min\{T_i(X), T_j(X)\} \leq T_e(X), \qquad X \in \gamma([0, L_i(S)]). \tag{18}$$

Proof. For $X = \gamma(s)$, the triangle inequality gives

$$L_{\mathcal{F}}(p_i, X) \leq s, \qquad L_{\mathcal{F}}(p_e, X) \geq D_i - s. \tag{19}$$

Before capture, $D_i \geq d_i > d_c$, so $d_c < \rho_i^{\text{path}} < D_i$. For $s \leq d_c$, Equation (13) gives $T_i(X) = 0 \leq T_e(X)$. For $d_c < s \leq \min\{L_i(S), \rho_i^{\text{path}}\}$, Equations (19) and (16) yield

$$T_i(X) \leq \frac{s - d_c}{V_p} \leq \frac{D_i - s}{V_e} \leq T_e(X). \tag{20}$$

Thus, $T_i(X) \leq T_e(X)$ for every $X = \gamma(s)$ with $0 \leq s \leq \min\{L_i(S), \rho_i^{\text{path}}\}$.

The remaining path from X to S has length $L_i(S) - s$. Using the triangle inequality and $[z + \delta]_+ \leq [z]_+ + \delta$ for $\delta \geq 0$, we obtain

$$\begin{aligned} T_j(X) &\leq T_j(S) + \frac{L_i(S) - s}{V_p}, \\ T_e(X) &\geq T_e(S) - \frac{L_i(S) - s}{V_e}. \end{aligned} \tag{21}$$

Consequently,

$$\begin{aligned} T_j(X) - T_e(X) &\leq -\beta_j(S) + \kappa\big(L_i(S) - s\big) \\ &= \kappa\big(\rho_i^{\text{path}} - s - \mu_{ij}(S)\big). \end{aligned} \tag{22}$$

If $\mu_{ij}(S) \geq 0$, the right-hand side is negative whenever $s > \rho_i^{\text{path}}$. Hence, every point on the path satisfies either $T_i(X) \leq T_e(X)$ or $T_j(X) < T_e(X)$, which proves Equation (18). □

Figure 4 illustrates the connecting path γ and the two arc-length intervals used in the proof. Section 3.2 evaluates these margins at predicted terminal configurations to construct the objective. Negative $\mu_{ij}(S)$ are penalized together with distance and control effort.

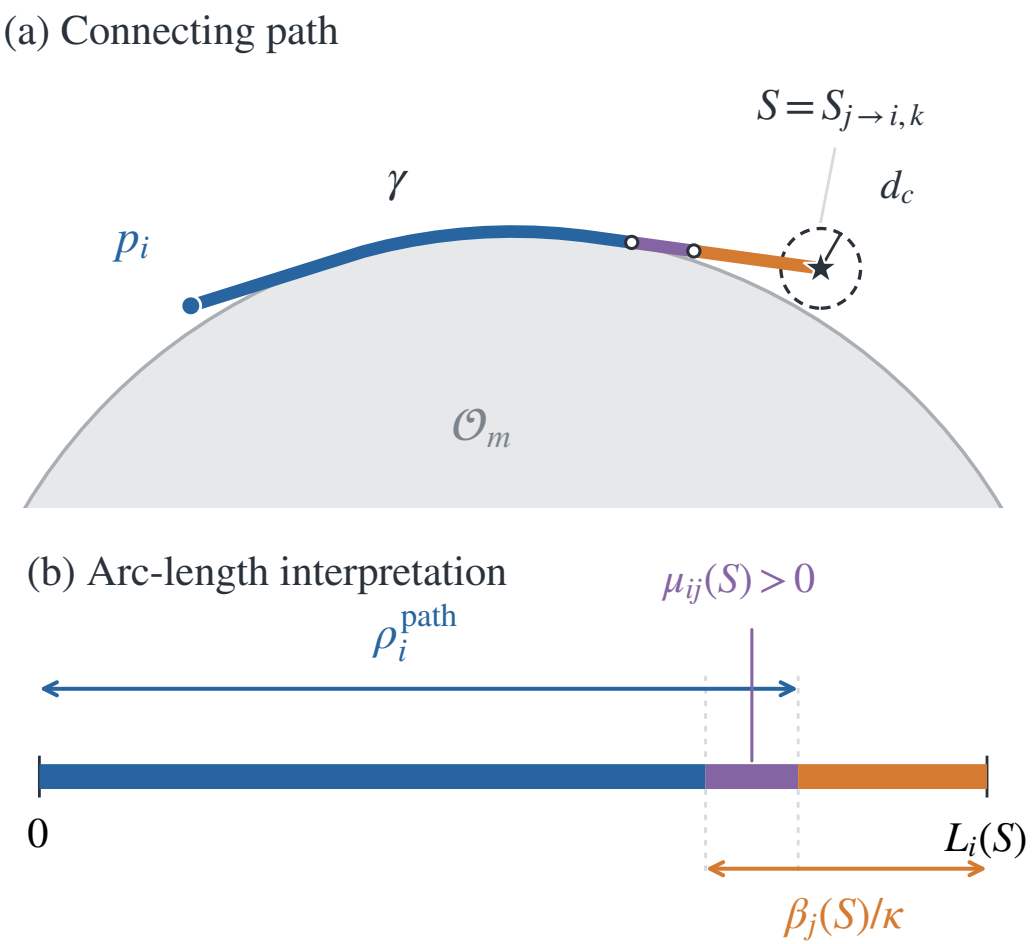


Figure 4. Geometric interpretation of Proposition 1. (**a**) A shortest collision-free path γ from p_i to the selected evaluation point $S = S_{j\to i,k}$, marked by a star. The dashed circle is centered at S and has radius d_c. (**b**) The corresponding intervals of s for $\beta_j(S) > 0$ and $\mu_{ij}(S) > 0$. The initial segment of length ρ_i^{path} (blue and purple) satisfies $T_i(X) \le T_e(X)$, while the terminal segment of length $\beta_j(S)/\kappa$ (orange and purple) satisfies $T_j(X) \le T_e(X)$. The purple overlap satisfies both inequalities and has length $\mu_{ij}(S)$ in the illustrated configuration.

Remark 3. *Proposition 1 establishes a local pairwise condition for geometric arrival advantage along the connecting path γ from p_i to the selected neighboring CO point $S_{j\to i,k}$. This path is a geometric construction and is not assumed to be the evader's trajectory. In the proposed planner, each pursuer evaluates the connection margins associated with both angular neighbors, $j \in \mathcal{N}_{i,k}$. The neighbor sets and evaluation points are updated at successive replanning instants. Thus, the criterion guides cooperation between angularly adjacent pursuers throughout the team as the configuration evolves.*

3.2. Distributed Receding-Horizon PSO–CBF Planning

At each planning instant t_k, pursuer P_i plans over $T = H\delta_p$, where δ_p is the prediction integration step and H is the number of prediction steps. The nominal replanning interval is denoted by Δ. Planning uses current measurements and the reference trajectories received from its angular neighbors. The neighbor set, evaluation points, and external predictions remain fixed during each local search.

3.2.1. Reference Prediction and Terminal Objective

Let $\mathbf{x}_{d,i} = [p_{d,i}^\top, \psi_{d,i}, u_{d,i}, v_{d,i}, r_{d,i}]^\top$ and $\mathbf{a}_{d,i} = [a_{u,d,i}, a_{r,d,i}]^\top$. The reference model is

$$\begin{aligned} \dot{p}_{d,i} &= R(\psi_{d,i}) \begin{bmatrix} u_{d,i} \\ v_{d,i} \end{bmatrix}, & \dot{\psi}_{d,i} &= r_{d,i}, \\ \dot{u}_{d,i} &= a_{u,d,i}, & \dot{r}_{d,i} &= a_{r,d,i}, \\ \dot{v}_{d,i} &= -a_v v_{d,i} - b_v u_{d,i} r_{d,i}. \end{aligned} \tag{23}$$

Each particle $\theta_i \in [-1,1]^{2n_b}$ encodes n_b pairs of acceleration values with search scales $D_a = \mathrm{diag}(a_u^{\mathrm{sc}}, a_r^{\mathrm{sc}}) \succ 0$. Smooth interpolation generates a proposal $\mathbf{a}_{d,i}^{\mathrm{raw}}(t;\theta_i)$, which is filtered before propagating Equation (23). The first reference is initialized from the measured state.

The neighbor predictions are obtained from their broadcast feasible references. The evader forecast follows Equation (4), with zero nominal normal acceleration filtered by its acceleration bound and obstacle HOCBFs based on $b_{e,m} = \|\hat{p}_e - o_m\|^2 - R_m^2$.

Let $p_{d,i,H|k}(\theta_i)$, $\bar{p}_{d,j,H|k}$, and $\hat{p}_{e,H|k}$ denote the corresponding terminal positions. For each fixed evaluation point $S_{j\to i,k}$, substitute these positions into Equation (17) and denote the resulting margin by $\widehat{\mu}_{ij,H|k}(\theta_i)$. The local objective is

$$\begin{aligned} J_{i,k}(\theta_i) = \sum_{j\in\mathcal{N}_{i,k}} \left[\frac{-\widehat{\mu}_{ij,H|k}(\theta_i)}{d_0}\right]_+^2 + \lambda_d \frac{\|p_{d,i,H|k}(\theta_i) - \hat{p}_{e,H|k}\|}{d_0} \\ + \frac{\lambda_a}{H} \sum_{h=0}^{H-1} \left\| D_a^{-1} \mathbf{a}_{d,i,h|k}(\theta_i) \right\|^2, \end{aligned} \tag{24}$$

where $d_0 > 0$, $\lambda_d > 0$, and $\lambda_a \geq 0$. The terms penalize negative connection margins, terminal target distance, and reference acceleration effort.

The prediction-state index h corresponds to $t_k + h\delta_p$, $h = 0, \ldots, H$, and the terminal index H corresponds to $t_k + T$. The pursuer reference states are obtained by numerical integration of the model in Equation (23), and the neighbor and evader predictions are evaluated on the same time grid. In the acceleration effort term, $\mathbf{a}_{d,i,h|k}(\theta_i)$ denotes the CBF-filtered acceleration sample computed during prediction integration step h, $h = 0, \ldots, H-1$.

3.2.2. CBF Projection for Reference Trajectories

Introduce $z_{d,i} = p_{d,i} + \ell q_{d,i}$, where $\ell > 0$, $q_{d,i} = q(\psi_{d,i})$, and $q_{d,i}^\perp = [-\sin\psi_{d,i}, \cos\psi_{d,i}]^\top$. Then

$$\begin{aligned} \dot{z}_{d,i} &= u_{d,i} q_{d,i} + (v_{d,i} + \ell r_{d,i}) q_{d,i}^\perp, \\ \ddot{z}_{d,i} &= F_{d,i} + G_{d,i} \mathbf{a}_{d,i}, \\ F_{d,i} &= R(\psi_{d,i}) \begin{bmatrix} -r_{d,i} v_{d,i} - \ell r_{d,i}^2 \\ -a_v v_{d,i} + (1 - b_v) u_{d,i} r_{d,i} \end{bmatrix}, \\ G_{d,i} &= R(\psi_{d,i})\, \mathrm{diag}(1, \ell). \end{aligned} \tag{25}$$

Thus, both $a_{u,d,i}$ and $a_{r,d,i}$ appear explicitly in $\ddot{z}_{d,i}$.

For obstacle m, let $s_{im} = z_{d,i} - o_m$ and define

$$h_{im} = \|s_{im}\|^2 - \rho_m^2, \qquad \rho_m = R_m + \ell. \tag{26}$$

Since $\dot{h}_{im} = 2s_{im}^{\top}\dot{z}_{d,i}$, the second-order condition $\ddot{h}_{im} + (\alpha_1 + \alpha_2)\dot{h}_{im} + \alpha_1\alpha_2 h_{im} \geq 0$ with $\alpha_1, \alpha_2 > 0$ becomes

$$2s_{im}^{\top}G_{d,i}\mathbf{a}_{d,i} + c_{im} \geq 0, \tag{27}$$

where $c_{im} = 2\|\dot{z}_{d,i}\|^2 + 2s_{im}^{\top}F_{d,i} + (\alpha_1 + \alpha_2)\dot{h}_{im} + \alpha_1\alpha_2 h_{im}$. With $h_{im}(t_k) \geq 0$ and $\dot{h}_{im}(t_k) + \alpha_1 h_{im}(t_k) \geq 0$, enforcing this condition preserves $h_{im} \geq 0$. Consequently, $\|p_{d,i} - o_m\| \geq \|z_{d,i} - o_m\| - \ell \geq R_m$.

The reference velocities are restricted by

$$\underline{U} \leq u_{d,i} \leq \overline{U}, \qquad |r_{d,i}| \leq \overline{R}, \qquad u_{d,i}^2 + v_{d,i}^2 \leq V_p^2. \tag{28}$$

Define the associated barrier functions

$$\mathcal{G}_i = \begin{Bmatrix} u_{d,i} - \underline{U}, & \overline{U} - u_{d,i}, \\ r_{d,i} + \overline{R}, & \overline{R} - r_{d,i}, \\ V_p^2 - u_{d,i}^2 - v_{d,i}^2 \end{Bmatrix}. \tag{29}$$

Their derivatives along Equation (23) are affine in $\mathbf{a}_{d,i}$. The acceleration proposal is projected by

$$\begin{aligned} \mathbf{a}_{d,i} = \arg\min_{\mathbf{a}\in\mathbb{R}^2} \; & \frac{1}{2}(\mathbf{a} - \mathbf{a}_{d,i}^{\text{raw}})^{\top} Q_a (\mathbf{a} - \mathbf{a}_{d,i}^{\text{raw}}) \\ \text{subject to} \; & 2s_{im}^{\top}G_{d,i}\mathbf{a} + c_{im} \geq 0, \quad m = 1, \ldots, M, \\ & \dot{g}(\mathbf{x}_{d,i}, \mathbf{a}) + \alpha_g g \geq 0, \quad g \in \mathcal{G}_i, \end{aligned} \tag{30}$$

where $Q_a \succ 0$ and $\alpha_g > 0$. From $g(t_k) \geq 0$, the first-order conditions preserve the reference velocity limits. The filtered input is used to propagate all reference states. The above constraint-preservation statements concern the reference model and require the stated initial barrier conditions, continued feasibility of Equation (30), and continuous enforcement of its constraints. The resulting obstacle-clearance guarantee applies to $p_{d,i}$; its relation to the actual position p_i is discussed in Remark 5. Infeasibility detection and handling are described in Section 4.1.

3.2.3. Local Search and Receding-Horizon Execution

The swarm is initialized using the shifted previous solution, zero parameters, and random samples. At iteration n, particle s of pursuer P_i is updated by

$$\begin{aligned} v_{i,s}^{n+1} &= \omega v_{i,s}^{n} + c_1 \zeta_{1,i,s}^{n} \odot \left(\theta_{i,s,\text{best}}^{n} - \theta_{i,s}^{n}\right) \\ &\quad + c_2 \zeta_{2,i,s}^{n} \odot \left(\theta_{i,\text{best}}^{n} - \theta_{i,s}^{n}\right), \\ \theta_{i,s}^{n+1} &= \text{proj}_{[-1,1]^{2n_b}}\left(\theta_{i,s}^{n} + v_{i,s}^{n+1}\right), \end{aligned} \tag{31}$$

where $v_{i,s}^{n}$ is the particle's search velocity, $\omega \geq 0$ is the inertia weight, and $c_1, c_2 > 0$ are learning coefficients. The entries of $\zeta_{1,i,s}^{n}$ and $\zeta_{2,i,s}^{n}$ are independent uniform samples on $[0, 1]$, and $\odot$ denotes componentwise multiplication. Here, $\theta_{i,s,\text{best}}^{n}$ and $\theta_{i,\text{best}}^{n}$ denote the particle's personal best and pursuer P_i's local swarm best, respectively.

For each candidate, CBF projection precedes reference propagation. Candidate trajectories are propagated until the prediction horizon or the first predicted capture, whichever occurs first.

After the prescribed iteration budget, the best feasible solution supplies the reference velocities $u_{d,i}, v_{d,i}, r_{d,i}$ and the corresponding $p_{d,i}$ and its derivatives to Section 3.3. The selected reference is used for tracking over $[t_k, t_{k+1})$ and updated at t_{k+1}, with a nominal replanning interval of Δ.

Algorithm 1 summarizes the local planning procedure for each pursuer. The numerical settings and feasibility tolerances are specified in Section 4.1.

Algorithm 1 Local RH–PSO–CBF planning for pursuer P_i

Input: Measurements, received positions and references, obstacle map, parameters, active reference, and previous solution.
Output: Selected feasible reference trajectory, or planner failure.
Initialization: Initialize the first reference from the measured state and the previous parameter vector to zero.
At each replanning instant t_k:
Preserve the current reference state and acceleration; update $\mathcal{N}_{i,k}$ and $S_{j\to i,k}$ by Definitions 2 and 4.
Form neighbor and evader predictions as in Section 3.2.1 on $t_k + h\delta_p$, $h = 0, \ldots, H$; hold uncovered neighbor tails at their final predicted positions.
Fix the neighbor set, evaluation points, and external predictions; initialize the swarm as in Section 4.1 with zero search velocities.
for each prescribed PSO iteration **do**
    for each particle θ_i **do**
        Form the smooth acceleration proposal with the preserved initial acceleration; start from the current reference state.
        Propagate Equation (23) with step δ_p until predicted capture or $t_k + T$, solving Equation (30) before each propagation; reject immediately on QP infeasibility or sampled reference-state constraint violation.
        Evaluate feasible noncapturing candidates by Equation (24).
    end for
    Update personal and local swarm bests, prioritizing feasible predicted-capture candidates.
    If another iteration remains, update particles by Equation (31).
end for
if a feasible candidate has been found **then**
    Select the best feasible candidate and store its reference and parameters.
else if the previous reference covers the next Δ and its next segment passes the δ_c-step feasibility check in Section 4.1 from the current reference state **then**
    Retain the previous reference.
else
    return planner failure.
end if
Share the selected reference and supply its reference velocities, position, and derivatives to the tracking layer in Section 3.3.
Repeat at t_{k+1} if pursuit continues.

3.3. Coordinated Surge–Yaw Control for Position Tracking

For each pursuer P_i, the reference velocities in Section 3.2 generate the position trajectory $p_{d,i}$ and its derivatives. The lower layer generates commands $u_{c,i}, \psi_{c,i}, r_{c,i}$ from the position error and compensates for disturbances using ESOs.

3.3.1. Disturbance Observation

For pursuer P_i, let $\tau_i = [\tau_{u,i}, \tau_{r,i}]^\top$ and $w_i = [w_{u,i}, w_{v,i}, w_{r,i}]^\top$. The dynamics in Equation (3) take the compact form

$$\dot{\nu}_i = f^0(\nu_i) + \mathsf{B}_\tau \tau_i + w_i, \qquad \mathsf{B}_\tau = \begin{bmatrix} 1/m_u & 0 \\ 0 & 0 \\ 0 & 1/m_r \end{bmatrix}, \tag{32}$$

where $f^0(\nu_i) = [f_u^0(\nu_i), f_v^0(\nu_i), f_r^0(\nu_i)]^\top$ collects the nominal drift terms of the surge, sway, and yaw equations, respectively, with the control-input and disturbance terms excluded.

Following the standard ESO construction [30], the observer for pursuer P_i is designed as

$$\begin{aligned} \dot{\hat{\nu}}_i &= f^0(\nu_i) + \mathsf{B}_\tau \tau_i + \hat{w}_i + 2\Omega(\nu_i - \hat{\nu}_i), \\ \dot{\hat{w}}_i &= \Omega^2(\nu_i - \hat{\nu}_i), \end{aligned} \tag{33}$$

where $\hat{\nu}_i$ and $\hat{w}_i$ estimate ν_i and w_i, respectively, and $\Omega = \mathrm{diag}(\omega_u, \omega_v, \omega_r) \succ 0$ specifies the observer bandwidths. The observer is initialized with $\hat{\nu}_i(t_0) = \nu_i(t_0)$ and $\hat{w}_i(t_0) = 0$ and runs continuously across replanning instants. The controller uses the measured velocities ν_i for feedback and the estimates $\hat{w}_i$ for disturbance compensation.

Under Assumption 1, the ESO in Equation (33) yields bounded disturbance estimation errors $\tilde{w}_i = w_i - \hat{w}_i$ [30].

3.3.2. Surge–Yaw Control Design

For pursuer P_i, define the tracking errors as

$$\begin{aligned} e_{p,i} &= p_i - p_{d,i}, \quad e_{\psi,i} = \psi_i - \psi_{c,i}, \\ e_{u,i} &= u_i - u_{c,i}, \quad e_{r,i} = r_i - r_{c,i}, \end{aligned} \tag{34}$$

where $u_{c,i}$, $\psi_{c,i}$, and $r_{c,i}$ are the commands constructed below.

Choose the desired planar velocity

$$\mathbf{v}_{c,i} = \dot{p}_{d,i} - k_p e_{p,i}, \qquad U_{c,i} = \|\mathbf{v}_{c,i}\|, \tag{35}$$

where $k_p > 0$. The surge and heading commands are selected as

$$\begin{aligned} u_{c,i} &= \sqrt{U_{c,i}^2 - v_i^2}, \\ \chi_{c,i} &= \mathrm{atan2}\big((\mathbf{v}_{c,i})_y, (\mathbf{v}_{c,i})_x\big), \\ \psi_{c,i} &= \chi_{c,i} - \mathrm{atan2}(v_i, u_{c,i}). \end{aligned} \tag{36}$$

The heading angles are evaluated on a continuous branch. These commands satisfy $R(\psi_{c,i})[u_{c,i}, v_i]^\top = \mathbf{v}_{c,i}$, so the measured sway velocity is incorporated into the position-guided command construction.

Let $J_2 = \begin{bmatrix} 0 & -1 \\ 1 & 0 \end{bmatrix}$. The position error dynamics can be expressed as

$$\begin{aligned} d_{\psi,i} &= \int_0^1 R(\psi_{c,i} + \sigma e_{\psi,i}) J_2 \begin{bmatrix} u_{c,i} \\ v_i \end{bmatrix} \mathrm{d}\sigma, \\ \dot{e}_{p,i} &= -k_p e_{p,i} + q(\psi_i) e_{u,i} + d_{\psi,i} e_{\psi,i}. \end{aligned} \tag{37}$$

The integral representation remains well defined at $e_{\psi,i} = 0$.

The derivatives of the desired velocity magnitude and direction are obtained from

$$\begin{aligned} \dot{\mathbf{v}}_{c,i} &= \ddot{p}_{d,i} - k_p \left(R(\psi_i) \begin{bmatrix} u_i \\ v_i \end{bmatrix} - \dot{p}_{d,i} \right), \\ \dot{U}_{c,i} &= \frac{\mathbf{v}_{c,i}^\top \dot{\mathbf{v}}_{c,i}}{U_{c,i}}, \\ \dot{\chi}_{c,i} &= \frac{(J_2 \mathbf{v}_{c,i})^\top \dot{\mathbf{v}}_{c,i}}{U_{c,i}^2}. \end{aligned} \tag{38}$$

Differentiating the heading command and using Equation (3) gives

$$\begin{aligned} g_{c,i} &= 1 - \frac{b_v u_i}{u_{c,i}}, \\ F_{c,i} &= \dot{\chi}_{c,i} + \frac{a_v v_i}{u_{c,i}} + \frac{v_i \dot{U}_{c,i}}{U_{c,i} u_{c,i}}, \\ \dot{e}_{\psi,i} &= g_{c,i} r_i - F_{c,i} + \frac{w_{v,i}}{u_{c,i}}. \end{aligned} \tag{39}$$

Accordingly, choose

$$r_{c,i} = \frac{F_{c,i} - \hat{w}_{v,i}/u_{c,i} - k_\psi e_{\psi,i} - d_{\psi,i}^\top e_{p,i}}{g_{c,i}}, \tag{40}$$

where $k_\psi > 0$. The term $d_{\psi,i}^\top e_{p,i}$ couples the heading command to the position error, while $\hat{w}_{v,i}$ compensates for the sway disturbance in the heading error dynamics.

To complete the backstepping design, introduce the ideal control inputs

$$\begin{aligned} \tau_{u,i}^\star &= m_u \big[- f_u^0(\nu_i) - w_{u,i} + \dot{u}_{c,i} - k_u e_{u,i} - q(\psi_i)^\top e_{p,i} \big], \\ \tau_{r,i}^\star &= m_r \big[- f_r^0(\nu_i) - w_{r,i} + \dot{r}_{c,i} - k_r e_{r,i} - g_{c,i} e_{\psi,i} \big], \end{aligned} \tag{41}$$

where $k_u, k_r > 0$. These expressions use the same commands as Equations (36) and (40) and serve as the ideal inputs for the subsequent analysis.

The control commands before actuator limiting are obtained by replacing the unknown disturbances with their ESO estimates:

$$\tau_i^{\mathrm{cmd}} = \left. \begin{bmatrix} \tau_{u,i}^\star \\ \tau_{r,i}^\star \end{bmatrix} \right|_{w_i = \hat{w}_i}. \tag{42}$$

The command derivatives are evaluated by the chain rule using Equations (3) and (33) and the reference trajectory derivatives, with unknown disturbances replaced by their ESO estimates. At each control instant, the surge input is evaluated first and used in the yaw-input calculation.

3.3.3. Tracking Stability Analysis

Define the control-input deviations

$$\Delta\tau_{u,i} = \tau_{u,i} - \tau_{u,i}^\star, \qquad \Delta\tau_{r,i} = \tau_{r,i} - \tau_{r,i}^\star. \tag{43}$$

Here, $\tau_{u,i}$ and $\tau_{r,i}$ denote the actual inputs applied after actuator limiting. These deviations account for the effects of disturbance estimation and actuator saturation on the applied control inputs.

Substituting $\tau_{u,i} = \tau_{u,i}^\star + \Delta\tau_{u,i}$ and $\tau_{r,i} = \tau_{r,i}^\star + \Delta\tau_{r,i}$ into Equation (3), together with Equations (37) and (40), yields

$$\begin{aligned} \dot{e}_{p,i} &= -k_p e_{p,i} + q(\psi_i) e_{u,i} + d_{\psi,i} e_{\psi,i}, \\ \dot{e}_{\psi,i} &= -k_\psi e_{\psi,i} - d_{\psi,i}^\top e_{p,i} + g_{c,i} e_{r,i} + \frac{\tilde{w}_{v,i}}{u_{c,i}}, \\ \dot{e}_{u,i} &= f_u^0(\nu_i) + \frac{\tau_{u,i}}{m_u} + w_{u,i} - \dot{u}_{c,i} \\ &= -k_u e_{u,i} - q(\psi_i)^\top e_{p,i} + \frac{\Delta\tau_{u,i}}{m_u}, \\ \dot{e}_{r,i} &= f_r^0(\nu_i) + \frac{\tau_{r,i}}{m_r} + w_{r,i} - \dot{r}_{c,i} \\ &= -k_r e_{r,i} - g_{c,i} e_{\psi,i} + \frac{\Delta\tau_{r,i}}{m_r}. \end{aligned} \tag{44}$$

Let

$$\varepsilon_i = \begin{bmatrix} \widetilde{w}_{v,i}/u_{c,i} \\ \Delta\tau_{u,i}/m_u \\ \Delta\tau_{r,i}/m_r \end{bmatrix}. \tag{45}$$

The sway-observer residual enters the heading error equation, whereas the surge and yaw implementation errors enter through the control-input deviations.

Assumption 3. *The reference trajectory is sufficiently smooth, with bounded derivatives. The nominal inertia ratio satisfies $b_v = m_u/m_v \neq 1$. The vehicle velocities satisfy the forward-operation bounds stated in Section 2.1. On the time interval considered, there exist constants $u_* > 0$ and $g_* > 0$ such that, for every pursuer, $U_{c,i}^2(t) - v_i^2(t) \geq u_*^2$, $|g_{c,i}(t)| = \left|1 - \frac{b_v u_i(t)}{u_{c,i}(t)}\right| \geq g_*$.*

These conditions imply $u_{c,i} \geq u_*$ and $U_{c,i} \geq u_*$ and keep $g_{c,i}$ uniformly separated from zero. Thus, they exclude the denominator singularities in the command construction. The required command sensitivities are bounded on bounded subsets of this nonsingular domain. These conditions are additional operating assumptions for the tracking analysis.

Proposition 2. *Under Assumptions 1 and 3, with $k_p, k_\psi, k_u, k_r > 0$, the tracking error system in Equation (44) satisfies an input-to-state stability estimate with respect to ε_i on the time interval considered. If these assumptions hold for all $t \geq t_0$, bounded ε_i yields uniformly ultimately bounded tracking errors, while $\varepsilon_i \equiv 0$ yields exponential convergence to zero.*

Proof. Consider

$$V_i = \frac{1}{2}\left(\|e_{p,i}\|^2 + e_{\psi,i}^2 + e_{u,i}^2 + e_{r,i}^2\right). \tag{46}$$

Substitution of Equation (44) cancels the position–surge, position–heading, and heading–yaw cross terms, giving

$$\begin{aligned} \dot{V}_i = & -k_p\|e_{p,i}\|^2 - k_\psi e_{\psi,i}^2 - k_u e_{u,i}^2 - k_r e_{r,i}^2 \\ & + \frac{e_{\psi,i}}{u_{c,i}}\widetilde{w}_{v,i} + \frac{e_{u,i}}{m_u}\Delta\tau_{u,i} + \frac{e_{r,i}}{m_r}\Delta\tau_{r,i}. \end{aligned} \tag{47}$$

The negative quadratic terms in Equation (47) dominate the residual terms whenever the tracking errors are sufficiently large relative to $\|\varepsilon_i\|$. Thus, V_i is an ISS Lyapunov function with respect to ε_i, and bounded residual inputs yield uniformly ultimately bounded tracking errors. □

Remark 4. *Let $\tau_{j,i}^{\mathrm{cmd}}$ denote the control command computed from Equation (42). The input applied to the USV is*

$$\tau_{j,i} = \min\left\{\tau_{j,\max}, \max\left\{\tau_{j,\min}, \tau_{j,i}^{\mathrm{cmd}}\right\}\right\}, \qquad j \in \{u, r\}.$$

Thus, when a calculated surge force or yaw moment exceeds its admissible range, the corresponding applied input is held at the respective upper or lower limit.

The control-input deviations in Equation (43) can then be written as

$$\Delta\tau_{j,i} = \left(\tau_{j,i}^{\mathrm{cmd}} - \tau_{j,i}^{\star}\right) + \left(\tau_{j,i} - \tau_{j,i}^{\mathrm{cmd}}\right), \qquad j \in \{u, r\},$$

where the second term represents the deviation caused by saturation and enters the residual input ε_i in the ISS analysis of Proposition 2. Persistent or substantial saturation may increase the tracking errors through the additional input deviation.

Remark 5. *The relation between reference and actual obstacle clearance follows from the position-tracking error $e_{p,i} = p_i - p_{d,i}$ defined in Equation (34). Since $z_{d,i} = p_{d,i} + \ell q_{d,i}$ and $\|q_{d,i}\| = 1$, the triangle inequality gives*

$$\begin{aligned}\|p_i - o_m\| - R_m &\geq \|p_{d,i} - o_m\| - R_m - \|e_{p,i}\| \\ &\geq \|z_{d,i} - o_m\| - (R_m + \ell) - \|e_{p,i}\|.\end{aligned}$$

Thus, a sufficient condition for nonnegative actual clearance is $\|p_{d,i} - o_m\| - R_m \geq \|e_{p,i}\|$ for every pursuer and obstacle throughout the motion. The second inequality provides the more conservative sufficient condition $\|z_{d,i} - o_m\| - (R_m + \ell) \geq \|e_{p,i}\|$. The inflation $\rho_m = R_m + \ell$ in Equation (26) accounts for the point offset and does not by itself reserve additional clearance for tracking errors.

These inequalities use the true vehicle position and quantify the clearance needed to accommodate the position-tracking error. They provide a conditional geometric relation. The tracking boundedness established in Proposition 2 alone does not certify that the required clearance condition holds throughout the sampled-data implementation in the presence of measurement errors.

4. Simulation Results

4.1. Simulation Setup

A closed-loop co-simulation platform is developed using Unity 2022.3.62f3c1, ROS Noetic, and MATLAB R2023a.Unity provides the three-dimensional water environment and executes the three-degree-of-freedom USV dynamics, including inertia, damping, surge–sway–yaw coupling, and the prescribed external disturbances. MATLAB implements the cooperative trajectory planner, nominal reference generation, extended state observers, and surge–yaw tracking controllers. ROS supports bidirectional exchange of vessel states and control commands between the two modules.

During simulation, Unity transmits time-stamped positions, headings, body-frame velocities, and yaw rates to MATLAB through ROS. The feedback signals are sampled and perturbed according to the measurement settings of each experiment. MATLAB uses these signals to update the planning, estimation, and tracking calculations and returns the surge forces and yaw moments to Unity. These inputs drive the USV dynamics and generate the states used in the next feedback cycle.

A representative pursuit scenario is considered with five USVs and 24 stationary circular obstacles. The diagonal inertia and linear diagonal damping coefficients are adopted from the USV model in [24] and listed in Table 1, consistent with the formulation in Section 2.1. The pursuer speed limit is $V_p = 1.2\,\mathrm{m/s}$, whereas the evader travels at $V_e = 1.35\,\mathrm{m/s}$, giving $\lambda = 0.889$. The capture radius is $d_c = 0.8\,\mathrm{m}$.

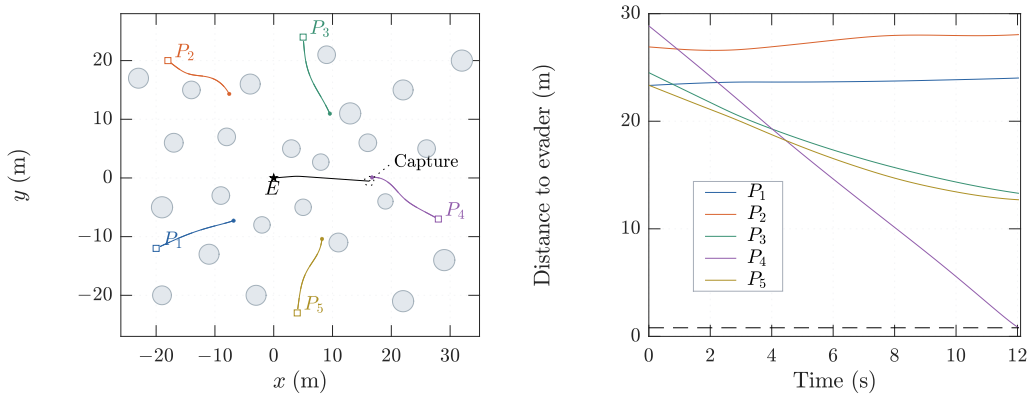
The initial pursuer positions are $(-20, -12)$, $(-18, 20)$, $(5, 24)$, $(28, -7)$, and $(4, -23)\,\mathrm{m}$. Their initial headings point towards $(7, 0.5)\,\mathrm{m}$, with an additional $-0.15\,\mathrm{rad}$ offset for P_4, and their initial body velocities are $(1.05, 0, 0)$. The evader starts at the origin with heading $0.08\,\mathrm{rad}$ and follows the obstacle-filtered prediction model, with normal acceleration bounded by $0.55\,\mathrm{m/s^2}$. The obstacle layout is shown in Figure 5a. The actual USV dynamics are subject to the following disturbances:

$$\begin{aligned}w_{u,i} &= 0.006 + 0.008\sin(0.45t + 0.4i), \\ w_{v,i} &= 0.004\sin(0.35t + 0.6i), \\ w_{r,i} &= 0.003\cos(0.4t + 0.3i).\end{aligned} \tag{48}$$

Here, $w_{u,i}$ and $w_{v,i}$ are acceleration disturbances in $\mathrm{m/s^2}$, and $w_{r,i}$ is an angular-acceleration disturbance in $\mathrm{rad/s^2}$, with t measured in seconds.

Table 1. Simulation parameters. Dimensional quantities are expressed in SI units.

Module	Parameters	Values
Vessel	m_u, m_v, m_r	25.8, 33.8, 2.76
	d_u, d_v, d_r	12, 17, 0.5
Reference bounds	$\underline{U}, \overline{U}, \overline{R}$	0.70, 1.18, 0.40
Actuator bounds	$\tau_{u,\min}, \tau_{u,\max}$	-30, 30
	$\tau_{r,\min}, \tau_{r,\max}$	-10, 10
Prediction	$T, \Delta, \delta_p, \delta_c$	6, 0.5, 0.15, 0.01
PSO	Swarm size, iterations, n_b	14, 7, 4
	ω, c_1, c_2	0.65, 1.5, 1.5
	$a_u^{\mathrm{sc}}, a_r^{\mathrm{sc}}$	0.12, 0.22
Objective	$d_0, \lambda_d, \lambda_a$	10, 100, 0.04
CBF	$\ell, \alpha_1, \alpha_2, \alpha_g$	0.65, 0.8, 0.8, 1.5
Tracking	k_p, k_ψ, k_u, k_r	0.5, 0.8, 1.1, 1.2
ESO	$\omega_u, \omega_v, \omega_r$	8, 8, 8



(**a**) Planar trajectories (**b**) Pursuer–evader distances

Figure 5. Representative pursuit under sampled measurement noise: (**a**) Actual trajectories, fixed obstacles, and initial positions. The black star marks the evader's initial position. (**b**) Actual pursuer–evader distances. The horizontal dashed line marks the capture threshold $d_c = 0.8\,\mathrm{m}$.

The main parameters are listed in Table 1. Reference prediction uses an integration step of $\delta_p = 0.15\,\mathrm{s}$ over a horizon $T = 6\,\mathrm{s}$, giving $H = T/\delta_p = 40$ prediction steps. During closed-loop execution, the nominal reference and ESO dynamics are integrated in MATLAB, whereas the USV dynamics are integrated in Unity using a custom implementation of the model in Section 2.1. Both modules use fourth-order Runge–Kutta integration with a maximum step of δ_c.

The modules are synchronized in simulation time. At each integration step, MATLAB uses the latest available sampled measurements, which are held between measurement updates. The planning module uses a nominal replanning interval of $\Delta = 0.5\,\mathrm{s}$. Measurement-noise levels and sampling periods are specified for each experiment. The reported simulations assume no message loss and no additional transmission delay.

Replanning preserves the active reference state and acceleration. Neighbor predictions are held fixed during each local search, with the last predicted position held constant over any uncovered forecast tail. The 14-particle swarm contains the time-shifted previous solution, a zero vector, two Gaussian perturbations of the shifted solution with componentwise standard deviation 0.15, and ten uniform samples from $[-1, 1]^{2n_b}$. The perturbed particles are clipped to this box. The previous parameter vector is initialized to zero at the first update, and all particle search velocities start at zero. Each local search terminates after seven iterations, corresponding to 98 candidate evaluations.

The obstacle-avoidance and reference-velocity inequalities in Equation (30) are checked jointly. The projection is treated as infeasible if no acceleration satisfying all these inequali-

ties within the specified QP feasibility tolerance is found. This includes conflicts between obstacle avoidance and the surge-speed, total-speed, or yaw-rate constraints.

Candidates with an infeasible CBF projection or a sampled reference-constraint violation are rejected. If no feasible candidate is found, the previous reference is retained only when its remaining horizon covers the next $\Delta = 0.5\,\mathrm{s}$ and the corresponding segment passes a feasibility check from the current reference state. This check uses a step of $\delta_c = 0.01\,\mathrm{s}$ and requires feasible CBF projections and satisfaction of the reference-state constraints at the integration stages. Otherwise, the run is terminated and recorded as a planner failure.

These numerical feasibility checks evaluate the reference constraints at the integration stages; they do not constitute a proof of constraint satisfaction between consecutive checking instants.

The reference trajectories and previous parameter vectors are initialized as described in Algorithm 1. MATLAB's Mersenne Twister generator is seeded once at the beginning of each trial and is not reset between replanning instants. The representative run uses seed 1019. The 55 matched trials per scenario in Section 4.3 use seeds 121,009–121,063, with the same seed used for Full, No TC, and No CM within each matched trial. The computational benchmark uses the seeds specified in Section 4.4. The QP weight is $Q_a = I_2$, and the CO evaluation-point search uses 61 angular samples when required. The state-constraint and QP feasibility tolerances are 2×10^{-3} and 10^{-9}, respectively.

Remark 6. *For efficiency, Dijkstra's algorithm is applied to the complete tangent graph of a subset of nearby obstacles. The subset is expanded and the shortest path recomputed whenever collisions with omitted obstacles are detected. Once the path is collision-free in the full environment, it is globally shortest, since omitting obstacles cannot increase the minimum path length.*

During prediction, candidate trajectories are truncated when the pursuer–evader distance first reaches d_c, and feasible trajectories meeting this condition are prioritized.

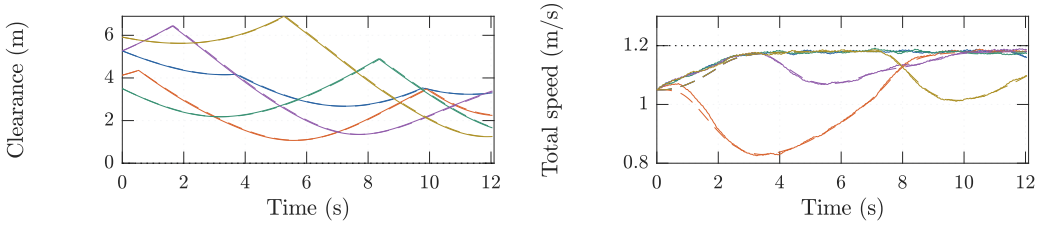
4.2. Cooperative Pursuit and Tracking in a Representative Scenario

The representative scenario examines the execution of the hierarchical controller by five underactuated USVs in the presence of 24 stationary circular obstacles. The initial deployment, model parameters, and smooth acceleration disturbances are those specified in Section 4.1. Sampled measurement noise is introduced into the position, heading, and body-velocity feedback. The Gaussian generating standard deviations are 0.02 m for each position component, 0.20° for heading, 0.001 m/s for each of the surge and sway velocities, and 0.01°/s for yaw rate. Each generated noise sample is clipped at three standard deviations. Position measurements are updated every 0.10 s, whereas heading and velocity measurements are updated every 0.02 s and held between updates. The control inputs are updated at intervals no greater than 0.01 s and held within each integration step. No additional network transmission delay is applied in this case.

Capture, clearance, and tracking statistics are evaluated from the simulated ground-truth states. Figure 5 shows the actual trajectories of the pursuers and the evader, together with the pursuer–evader distances. The pursuers follow different routes through the obstacle field, and P_4 reaches the capture disk at $t_c = 12.047\,\mathrm{s}$. Capture is located within the final integration interval, and the trajectory records end at this event.

The obstacle clearances and motion variables are shown in Figure 6. The minimum actual pursuer clearance, computed as $\min_{i,m,t}(\|p_i(t) - o_m\| - R_m)$, is 1.069 m. Here, R_m denotes the effective obstacle radius used by the planner, including the prescribed geometric clearance. No entry into an effective obstacle disk occurs before capture. The maximum reference and actual total speeds are 1.1800 m/s and 1.1918 m/s, respectively. Both the reference and actual total speeds remain below the prescribed limit of 1.20 m/s throughout

the simulated pursuit. As shown in Figure 6b, the actual total-speed profiles closely follow their respective references during acceleration and deceleration, with small deviations under sampled measurement noise.



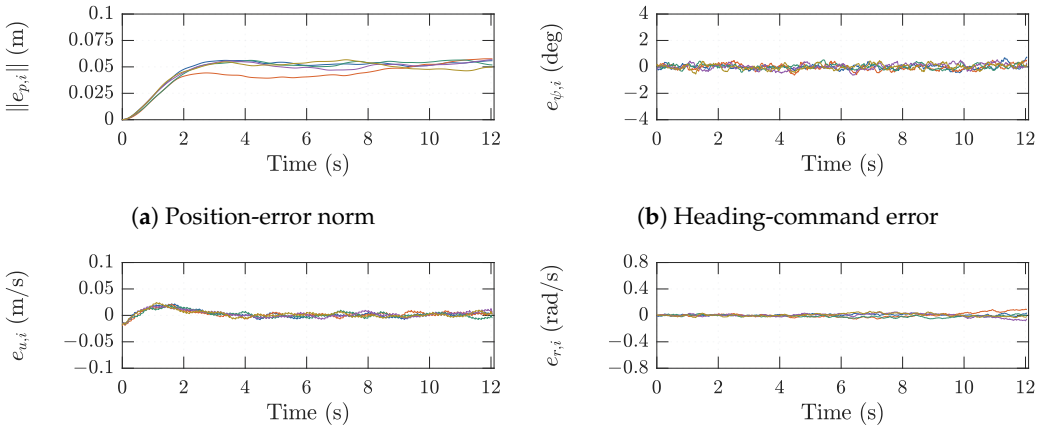
(**a**) Obstacle clearance (**b**) Total speed

Figure 6. Reference (dashed) and actual (solid) motion in the representative case. The colors identify the individual pursuers (P_1–P_5) as in Figure 5b: (**a**) minimum clearance from the effective obstacle disks; (**b**) total speed. The dotted lines indicate zero clearance in (**a**) and the prescribed speed limit V_p in (**b**).

Figure 7 reports the position error and the heading, surge, and yaw-rate errors in Equation (34). The heading error is wrapped to $(-\pi, \pi]$ for reporting. The maximum position error is 0.0577 m, and the overall position root-mean-square error is 0.0480 m. The latter is computed over the $N_s = 1204$ recorded time instants as

$$E_{p,\mathrm{RMS}} = \left[\frac{1}{N N_s} \sum_{i=1}^{N} \sum_{\ell=1}^{N_s} \| p_i(t_\ell) - p_{d,i}(t_\ell) \|^2 \right]^{1/2}. \tag{49}$$

The nonzero errors include the effects of measurement noise, the sample holding, and the prescribed process disturbances. In particular, the surge and yaw-rate errors are computed relative to $u_{c,i}$ and $r_{c,i}$ generated by the position controller, consistently with the lower-layer design. The position-error profiles indicate satisfactory tracking of the nominal trajectories by the underactuated USVs in this scenario.



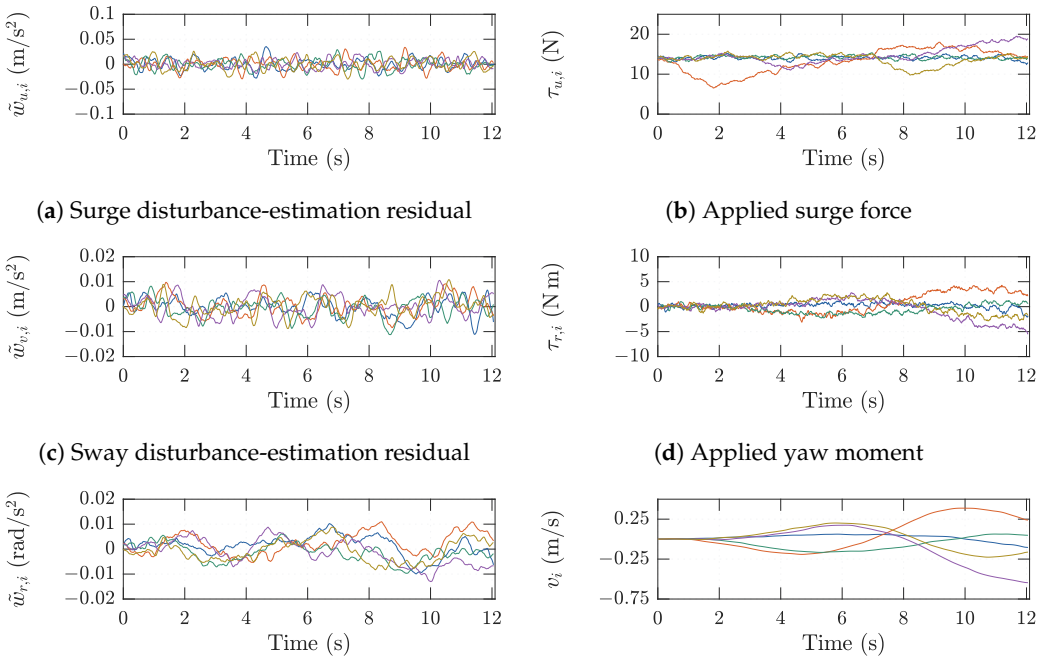
(**a**) Position-error norm (**b**) Heading-command error

(**c**) Surge-command error (**d**) Yaw-rate-command error

Figure 7. Tracking errors evaluated from the simulated ground-truth states: (**a**) position-error norm; (**b**) wrapped heading-command error; (**c**) surge-command error; (**d**) yaw-rate-command error.

The ESO residuals, applied inputs, and sway velocities are presented in Figure 8. For visual clarity, the curves are displayed using a centered moving average with a 0.20 s window, while all reported statistics are computed from the unfiltered data. Over the recorded samples with $t \geq 2$ s, the RMS disturbance-estimation residuals in the surge, sway, and yaw channels are 0.0163 m/s^2, 0.0046 m/s^2, and 0.0050 rad/s^2, respectively. As shown

in Figure 8, the surge-force and yaw-moment inputs remain within their prescribed bounds throughout the pursuit process. The sway velocity is retained as an unactuated state and is not assigned an independent tracking command.



(**a**) Surge disturbance-estimation residual

(**b**) Applied surge force

(**c**) Sway disturbance-estimation residual

(**d**) Applied yaw moment

(**e**) Yaw disturbance-estimation residual

(**f**) Actual sway velocity

Figure 8. Lower-layer responses: (**a**,**c**,**e**) disturbance-estimation residuals in surge, sway, and yaw; (**b**) applied surge force; (**d**) applied yaw moment; (**f**) actual sway velocity. Disturbance truth is used only to evaluate the observer residuals offline.

Figure 9 illustrates the pursuit routes, obstacle-avoidance motion, and final capture in the Unity simulation. Panel (a) shows the recorded trajectories from the initial time to capture. Panel (b) shows P_4 reaching the capture threshold $d_c = 0.8\,\mathrm{m}$ at $t_c = 12.047\,\mathrm{s}$.

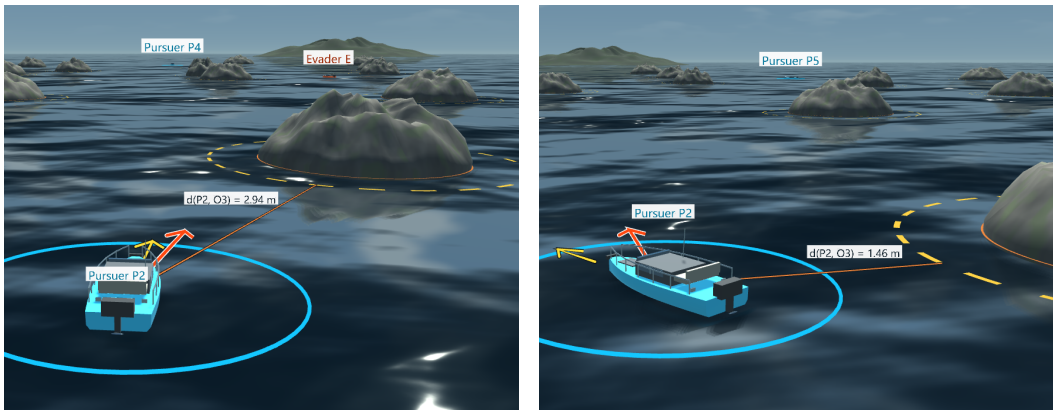
Panels (c) and (d) show P_2 approaching and moving away from obstacle O_3 at $t = 2\,\mathrm{s}$ and $t = 7\,\mathrm{s}$, respectively, with the corresponding distances marked in the images. The yellow arrows indicate P_2's direction of motion, while the red arrows indicate the direction toward the evader. Their different orientations in panel (d) illustrate how P_2 adjusts its motion near the obstacle while continuing the pursuit. These views complement the quantitative trajectory and obstacle-clearance results.



(**a**) Full pursuit trajectories

(**b**) Capture by P_4 at $t_c = 12.047\,\mathrm{s}$

Figure 9. *Cont.*



(**c**) P_2 approaching O_3 at $t = 2\,\mathrm{s}$ (**d**) P_2 moving away from O_3 at $t = 7\,\mathrm{s}$

Figure 9. Pursuit, obstacle avoidance, and capture in the Unity simulation: (**a**) recorded trajectories from the initial time to capture, with cyan and orange-red curves denoting the pursuers and the evader, respectively; (**b**) capture by P_4, with a displayed separation of 0.80 m; (**c**,**d**) P_2 approaching and moving away from obstacle O_3, with clearances of 2.94 m and 1.46 m, respectively. In both panels, the yellow arrows show P_2's direction of motion, and the red arrows point toward the evader.

4.3. Neighboring Time Compensation and Ablation Analysis

The complete method (Full) is compared with an ablation (No TC) that removes only the signed neighboring contribution while retaining the own path margin. Let $a_{ij} = \widehat{\rho}_i^{\mathrm{path}} - \widehat{L}_i(S)$ and $b_{ij} = \widehat{\beta}_j(S)/\kappa$ in the terminal-prediction context. The corresponding penalties are

$$J_{\mu,i}^{\mathrm{Full}} = \sum_j \left[\frac{-(a_{ij}+b_{ij})}{d_0}\right]_+^2, \qquad J_{\mu,i}^{\mathrm{No\ TC}} = \sum_j \left[\frac{-a_{ij}}{d_0}\right]_+^2. \tag{50}$$

A positive b_{ij} reduces an own-margin deficit, whereas a negative value increases it. These quantities guide the relative planning emphasis assigned to neighboring connections. The evaluation-point selection rule, remaining objective terms, CBF projection, and tracking controller are unchanged. The USV model, process disturbances, planning settings, and tracking gains follow Section 4.1.

Two scenarios with nonuniform pursuer deployments and asymmetric obstacle layouts are used to evaluate the benefits of the proposed neighboring time-compensation mechanism through matched ablation experiments. Scenario 1 contains eight obstacle disks, with six to the left of the initial evader position and two to its right. The evader follows the obstacle-avoiding policy at 1.40 m/s. Scenario 2 adopts a second asymmetric obstacle configuration, with modified obstacle positions and radii, and a reactive evader traveling at 1.48 m/s. The evader adjusts its heading in response to nearby pursuers, subject to the prescribed maneuvering limits and obstacle-avoidance constraints. The reactive policy uses true pursuer positions to generate the simulated evader's actual motion. It adds a weighted sum of unit vectors pointing from each pursuer toward the evader to the unit vector along the evader's initial heading. The weight associated with pursuer i is $k_e \exp[-(\|p_e - p_i\|/(15))^2]$. The resulting vector determines the desired heading, limited to within 0.6 rad of the initial heading. The evader turns toward this heading subject to the obstacle-avoidance and acceleration constraints. The baseline Scenario 2 uses $k_e = 1$ and $|a_e| \le 0.55\,\mathrm{m/s^2}$, corresponding to a turning-rate bound of $\bar{\omega}_e = 0.55/1.48 \approx 0.372\,\mathrm{rad/s}$. The pursuers predict the evader's motion using the zero-nominal-acceleration model with obstacle filtering, without incorporating the reactive policy.

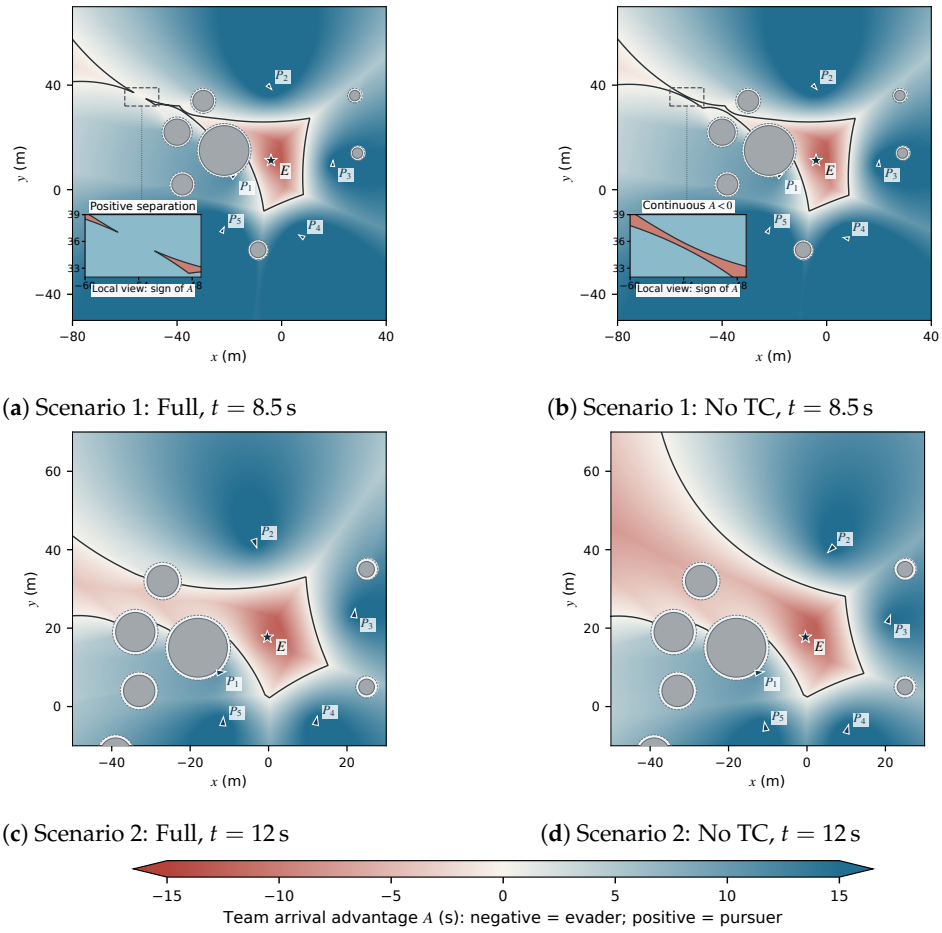
4.3.1. Arrival Advantage Comparison

To compare the estimated arrival times of the evader and the pursuers, we define the team arrival advantage as

$$\begin{aligned} A(X,t) &= T_e(X;t) - \min_{1\le i\le N} T_i(X;t), \\ T_e(X;t) &= \frac{L_{\mathcal{F}}(p_e(t),X)}{V_e}, \qquad T_i(X;t) = \frac{[L_{\mathcal{F}}(p_i(t),X) - d_c]_+}{V_p}, \end{aligned} \tag{51}$$

where $X \in \mathcal{F}$. A positive value indicates that at least one pursuer has a shorter estimated arrival time than the evader and a negative value favors the evader. These estimates use the shortest collision-free path lengths and account for the capture radius. Turning and tracking effects are evaluated through the dynamic simulation.

Figure 10 presents two matched examples: Scenario 1 at $t = 8.5$ s and Scenario 2 at $t = 12$ s. The rows refer to separate paired trials, each sharing the same initial states and simulation conditions between Full and No TC. All maps are reconstructed from simulated true positions and use the same color scale. The coordinate ranges are identical for Full and No TC within each row. The second row uses a smaller plotting window to highlight the differences in the evader-favored region. We compare the extent of the region with $A < 0$ connected to the evader's current position.



(**a**) Scenario 1: Full, $t = 8.5$ s

(**b**) Scenario 1: No TC, $t = 8.5$ s

(**c**) Scenario 2: Full, $t = 12$ s

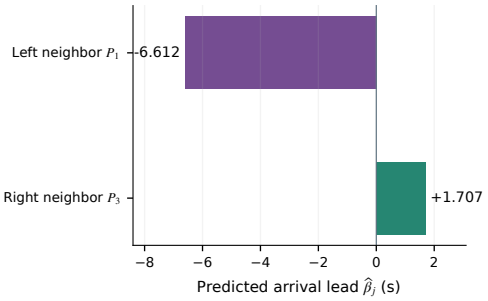
(**d**) Scenario 2: No TC, $t = 12$ s

Figure 10. Team arrival advantage in two matched examples: (**a**,**b**) Scenario 1 at $t = 8.5$ s; (**c**,**d**) Scenario 2 at $t = 12$ s. Red and blue indicate negative and positive A, respectively, and black contours denote $A = 0$. Gray disks are effective obstacles. The star labeled E marks the evader's position. Insets in (**a**,**b**) display the sign of A in the same boxed region. Coordinate ranges are identical within each row, with a closer view in (**c**,**d**). All main panels share the color scale shown below.

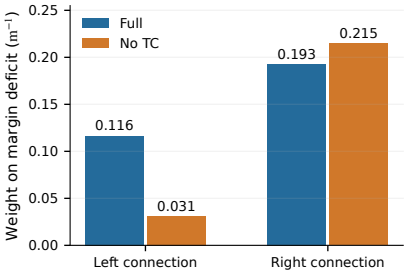
In Scenario 1 at $t = 8.5$ s, the region with $A < 0$ connected to the evader is bounded under Full. Under No TC, it extends toward the upper left through a narrow passage. The insets highlight this difference. The same pattern is obtained with grid spacings of 0.25 and 0.125 m and is confirmed by direct checks of the separating boundary and connecting path.

In Scenario 2 at $t = 12$ s, the negative region connected to the evader extends farther toward the upper left under No TC. Under Full, a larger part of this area has $A > 0$, indicating an arrival advantage for the pursuers. Although an outward negative connection is present under both methods, the evader-favored region within the displayed window is noticeably smaller under Full.

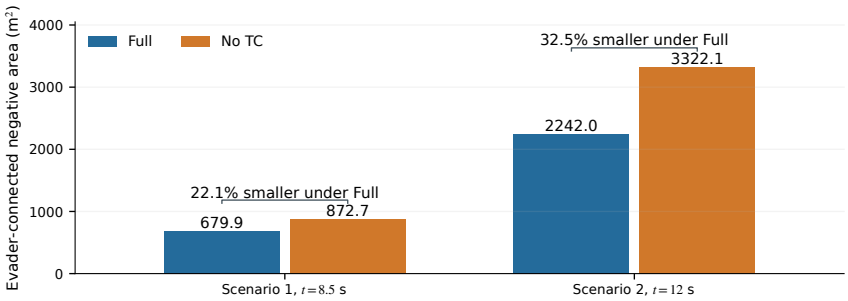
Figure 11a,b shows how compensation changes the planning emphasis of P_2 at the initial update in Scenario 1. The left neighbor P_1 has a predicted arrival delay of 6.612 s, while the right neighbor P_3 has a lead of 1.707 s. At the same candidate, compensation increases the penalty sensitivity $|\partial J_{\mu,i}/\partial a_{ij}|$ for the left connection and decreases it for the right, giving greater emphasis to the delayed neighbor.



(**a**) Neighbor arrival-time differences



(**b**) Penalty sensitivities



(**c**) Areas of the evader-connected negative region

Figure 11. Neighboring time compensation: (**a**) predicted arrival differences of P_2's neighbors at the initial update in Scenario 1; (**b**) penalty sensitivities at the same candidate; (**c**) areas of the negative region connected to the evader, evaluated within a common window. Percentages indicate reductions under Full relative to No TC.

Figure 11c compares the areas of the region with $A < 0$ connected to the evader. All areas are computed on a 0.125 m grid within the same window $[-80, 40] \times [-50, 70]$ m^2. Compared with No TC, Full reduces the area from 872.7 to 679.9 m^2 in Scenario 1 at 8.5 s and from 3322.1 to 2242.0 m^2 in Scenario 2 at 12 s, corresponding to reductions of 22.1% and 32.5%, respectively.

In these examples, Full captures the evader at 21.500 and 20.901 s, respectively, whereas No TC does not capture within 40 s.

4.3.2. Capture Performance Comparison

An additional ablation (No CM) omits the entire first term in Equation (24). Table 2 compares Full, No TC, and No CM over 55 matched trials per scenario, giving 330 runs in

total. Within each matched trial, the three methods use identical initial conditions, random seeds, and all other settings. All runs are included, with time limits and planner failures reported separately. Runs that reach the 40 s simulation time limit without capture are recorded as unsuccessful capture trials. A planner failure occurs when the search finds no feasible candidate and no usable previous reference remains.

Table 2. Matched ablation results for the two scenarios. Capture times are reported as medians [interquartile ranges] over successful trials only.

Scenario	Method	Capture Rate (n_c/55)	Time Limits	Planner Failures	t_c (s)
1	Full	0.891	4	2	21.405 [21.250, 21.798]
1	No TC	0.564	20	4	21.742 [21.640, 22.365]
1	No CM	0.473	27	2	19.455 [19.158, 20.037]
2	Full	1.000	0	0	20.916 [20.888, 20.957]
2	No TC	0.509	24	3	20.989 [20.957, 21.032]
2	No CM	0.418	29	3	18.522 [18.363, 18.706]

All 55 matched pairs are included in each scenario, with time-limit terminations and planner failures treated as unsuccessful outcomes. We compare the numbers of pairs in which only Full succeeds and only No TC succeeds. For pairs in which only one method succeeds, the two possible outcomes are equally likely under the hypothesis of equal capture probabilities. The two-sided exact p-value is therefore calculated using a binomial distribution with probability $1/2$ and the number of these pairs as the trial count.

In Scenario 1, only Full succeeds in 21 matched pairs, whereas only No TC succeeds in 3 pairs, yielding $p = 2.77 \times 10^{-4}$. The corresponding counts in Scenario 2 are 27 and 0, respectively, with $p = 1.49 \times 10^{-8}$.

Full achieves a higher capture rate than No TC in both scenarios, while the median capture times among successful trials remain close. Together with the arrival-advantage comparisons above, these results indicate that neighboring time compensation improves capture success in the two tested scenarios with unevenly distributed obstacles and pursuers. No CM achieves capture rates of 47.3% and 41.8% in Scenarios 1 and 2, respectively, both below those of Full and No TC, supporting the contribution of the connection-margin penalty to capture success in these tests. Although No CM has shorter median capture times, these values are calculated over different subsets of successful trials and should be interpreted together with its lower capture rates.

Additional tests retain the Scenario 2 geometry and use the Full method. We vary $k_e \in \{0, 0.5, 1, 2\}$ with the original acceleration bound of $0.55\,\mathrm{m/s^2}$. The target predictor is unchanged in every condition, including its $0.55\ \mathrm{m/s^2}$ acceleration bound. All four conditions use the same 26 random seeds (10056–10081), which differ from those used in the preceding ablation experiments. The position-prediction RMSE at lead time T_f is

$$E_{T_\mathrm{f}} = \left(\frac{1}{|\mathcal{I}_{T_\mathrm{f}}|} \sum_{(n_\mathrm{tr},k)\in\mathcal{I}_{T_\mathrm{f}}} \left\| \hat{p}_e^{(n_\mathrm{tr})}(t_k + T_\mathrm{f} \mid t_k) - p_e^{(n_\mathrm{tr})}(t_k + T_\mathrm{f}) \right\|^2 \right)^{1/2}, \qquad T_\mathrm{f} \in \{0.5, 6\}\,\mathrm{s},$$

where n_tr indexes trials and $\mathcal{I}_{T_\mathrm{f}}$ contains only forecast origins with a recorded future true state. Table 3 reports these errors, capture counts, minimum actual pursuer–obstacle clearance, and obstacle-entry events.

With the predictor unchanged, increasing k_e from 0 to 2 raises the 6 s position-prediction RMSE from 0.043 m to 1.505 m, while the 0.5 s RMSE remains approximately 0.03 m. The empirical capture rate decreases from 100% to 88.5%, indicating sensitivity to stronger unmodeled reactive maneuvers. No obstacle-entry events are observed, and the minimum actual pursuer–obstacle clearance across all conditions is 0.744 m. Thus, capture

performance decreases under the tested maneuvers, while positive obstacle clearance is maintained over the recorded trajectories.

Table 3. Effects of unmodeled evader maneuvers on prediction accuracy, capture success, and obstacle clearance in Scenario 2.

k_e	$E_{0.5}$ (m)	E_6 (m)	Capture Rate (n_c/26)	Min Clearance (m)	N_{obs}
0	0.028	0.043	1.000	0.744	0
0.5	0.029	0.599	1.000	0.773	0
1	0.031	0.780	0.962	0.765	0
2	0.031	1.505	0.885	0.749	0

4.4. Computational Performance

Computational performance was evaluated on a Windows 11 computer with an Intel Core i5-12400F processor and approximately 8 GB of RAM. The wall-clock time of each complete local planning update for an individual USV was measured directly, from processing the available state and reference data to preparing the updated reference for transmission. The measurement includes neighbor selection, target and neighbor prediction, PSO search, path-graph construction and shortest-path queries, and CBF constraint projection.

Five random seeds, 1019–1023, were used for each configuration. The tests vary the obstacle count $M \in \{12, 24, 36\}$ with $N = 5$ pursuers and the pursuer count $N \in \{3, 5, 8\}$ with $M = 24$, while keeping the PSO and reference-prediction settings fixed. Table 4 reports the mean, empirical 95th percentile (P95), and maximum observed computation time, pooled over the completed local updates from all pursuers and seeds in each configuration.

Table 4. Wall-clock time per complete local planning update for an individual USV. All times are in milliseconds.

N	M	Completed Local Updates	Mean	P95	Maximum Observed
5	12	585	81.70	142.27	180.58
5	24	605	98.82	164.27	233.13
5	36	632	127.39	216.30	262.74
3	24	381	114.66	197.75	321.32
8	24	976	92.97	157.03	225.38

For $N = 5$ and $M = 24$, the mean, empirical 95th-percentile, and maximum observed computation times per local update are 98.82, 164.27, and 233.13 ms, respectively. The maximum observed time is below the nominal replanning interval of $\Delta = 0.5$ s, supporting the per-USV planning computation budget under the tested configuration and hardware. The mean times spent on path-graph construction and CBF processing are 6.54 and 64.82 ms per local update, respectively. QP projection accounts for 14.88 ms of the CBF processing time.

The main local workload consists of 98 candidate evaluations, each with at most $H = 40$ prediction steps and a fixed number of terminal path queries when required. Increasing M increases obstacle-related constraint processing and can enlarge the tangent graphs used for geometric distance evaluation. For $M = 24$, the results show higher mean planning times per USV with fewer pursuers. Although each pursuer still uses two angular neighbors, changing N can alter the neighbor configuration and the associated evaluation points. Even with the same obstacle map, these geometric changes may increase the proportion of distance queries requiring obstacle detours and tangent-graph searches, providing a possible explanation for the observed timing differences.

5. Conclusions

This study developed a hierarchical cooperative pursuit framework for underactuated USVs facing a faster evader in obstacle environments. The signed path-connection margin quantifies neighboring time compensation and provides a sufficient condition for collective geometric arrival advantage along a collision-free connecting path. Evaluating this margin on CBF-filtered predictions allows nominal trajectory optimization to account for obstacle-induced detours and safety corrections. Under the stated assumptions, the tracking analysis establishes uniformly ultimately bounded tracking errors in the presence of bounded observation and control-input residuals.

In the representative scenario with sampled measurement noise and time-varying disturbances, five pursuing USVs captured the faster evader among 24 stationary circular obstacles at 12.047 s. The minimum clearance from the effective obstacle disks was 1.069 m, and the maximum position-tracking error was 0.0577 m. Matched ablation experiments in two scenarios with nonuniform obstacle and pursuer distributions showed higher observed capture rates with neighboring time compensation, while capture times among successful trials remained comparable. These results demonstrate the contribution of neighboring arrival-time differences to cooperative pursuit under unequal travel-time requirements.

The present validation is limited to numerical simulations under the adopted USV model and tested operating conditions. Physical experiments are included in our future research plan, beginning with single-USV trajectory tracking and obstacle avoidance in a laboratory tank or controlled water environment. Subsequent multi-USV experiments will evaluate cooperative capture of a faster target, using capture success, obstacle clearance, and tracking accuracy as performance measures. These experiments will further assess the effects of localization errors, communication delays, environmental disturbances, and more varied evader maneuvers.

Author Contributions: Z.C.: conceptualization; methodology; software; validation; formal analysis; investigation; data curation; visualization; writing—original draft preparation. Z.L.: writing—review and editing. W.W.: supervision. All authors have read and agreed to the published version of the manuscript.

Funding: This research received no external funding.

Data Availability Statement: The simulation code and the data supporting the reported results will be made available by the corresponding author on reasonable request.

Conflicts of Interest: The authors declare no conflicts of interest.

References

1. Liu, Z.; Zhang, Y.; Yu, X.; Yuan, C. Unmanned surface vehicles: An overview of developments and challenges. *Annu. Rev. Control* **2016**, *41*, 71–93. https://doi.org/10.1016/j.arcontrol.2016.04.018.
2. Yan, R.; Deng, R.; Duan, X.; Shi, Z.; Zhong, Y. Multiplayer Reach-Avoid Differential Games with Simple Motions: A Review. *Front. Control Eng.* **2023**, *3*, 1093186. https://doi.org/10.3389/fcteg.2022.1093186.
3. Fang, B.; Pan, Q.; Hong, B.; Ding, L.; Cai, Z. Constraint Conditions of Successful Capture in Multi-Pursuers vs One-Evader Games. *Robot* **2012**, *34*, 282–291. (In Chinese) https://doi.org/10.3724/SP.J.1218.2012.00282.
4. Ramana, M.V.; Kothari, M. Pursuit Strategy to Capture High-Speed Evaders Using Multiple Pursuers. *J. Guid. Control. Dyn.* **2017**, *40*, 139–149. https://doi.org/10.2514/1.G000584.
5. Fang, X.; Wang, C.; Xie, L.; Chen, J. Cooperative Pursuit With Multi-Pursuer and One Faster Free-Moving Evader. *IEEE Trans. Cybern.* **2022**, *52*, 1405–1414. https://doi.org/10.1109/TCYB.2019.2958548.
6. Zha, W.; Chen, J.; Peng, Z.; Gu, D. Construction of Barrier in a Fishing Game With Point Capture. *IEEE Trans. Cybern.* **2017**, *47*, 1409–1422. https://doi.org/10.1109/TCYB.2016.2546381.
7. Chen, J.; Zha, W.; Peng, Z.; Gu, D. Multi-Player Pursuit–Evasion Games with One Superior Evader. *Automatica* **2016**, *71*, 24–32. https://doi.org/10.1016/j.automatica.2016.04.012.

8. Cao, Z.; Liu, Z.; Ge, F.; Yu, J.; Wang, W.; Chen, Y. Cooperative fishing pursuit strategy for encirclement of a faster evader: Theory and application. *Int. J. Syst. Sci.* **2025**, 1–19. https://doi.org/10.1080/00207721.2025.2606900.
9. Garcia, E.; Bopardikar, S.D. Cooperative Containment of a High-Speed Evader. In Proceedings of the 2021 American Control Conference (ACC), New Orleans, LA, USA, 25–28 May 2021; pp. 4698–4703. https://doi.org/10.23919/ACC50511.2021.9483097.
10. Zhou, S.; Li, H.; Wu, T.; Sun, C. Containment Strategies for Heterogeneous Pursuers to Capture an Evader with Higher Speed. *J. Guid. Control. Dyn.* **2024**, *47*, 1241–1248. https://doi.org/10.2514/1.G007922.
11. Liu, Y.H.; Arimoto, S. Path Planning Using a Tangent Graph for Mobile Robots Among Polygonal and Curved Obstacles: Communication. *Int. J. Robot. Res.* **1992**, *11*, 376–382. https://doi.org/10.1177/027836499201100409.
12. Chen, D.Z.; Wang, H. Computing Shortest Paths among Curved Obstacles in the Plane. *ACM Trans. Algorithms* **2015**, *11*, 1–46. https://doi.org/10.1145/2660771.
13. Zhou, S.; Li, H.; Wu, T. Cooperative Containment Strategies to Pursue One Faster Evader with Collision Avoidance. *Unmanned Syst.* **2025**, *13*, 1481–1490. https://doi.org/10.1142/S230138502541002X.
14. Ames, A.D.; Xu, X.; Grizzle, J.W.; Tabuada, P. Control Barrier Function Based Quadratic Programs for Safety Critical Systems. *IEEE Trans. Autom. Control* **2017**, *62*, 3861– 3876. https://doi.org/10.1109/TAC.2016.2638961.
15. Nguyen, Q.; Sreenath, K. Exponential Control Barrier Functions for Enforcing High Relative-Degree Safety-Critical Constraints. In Proceedings of the 2016 American Control Conference (ACC), Boston, MA, USA, 6–8 July 2016; pp. 322–328. https://doi.org/10.1109/ACC.2016.7524935.
16. Xiao, W.; Belta, C. Control Barrier Functions for Systems with High Relative Degree. In Proceedings of the 2019 IEEE 58th Conference on Decision and Control (CDC), Nice, France, 11–13 December 2019; pp. 474–479. https://doi.org/10.1109/CDC40024.2019.9029455.
17. Xiao, W.; Belta, C. High-Order Control Barrier Functions. *IEEE Trans. Autom. Control* **2022**, *67*, 3655–3662. https://doi.org/10.1109/TAC.2021.3105491.
18. Chen, Y.; Singletary, A.; Ames, A.D. Guaranteed Obstacle Avoidance for Multi-Robot Operations With Limited Actuation: A Control Barrier Function Approach. *IEEE Control Syst. Lett.* **2021**, *5*, 127–132. https://doi.org/10.1109/LCSYS.2020.3000748.
19. Mestres, P.; Nieto-Granda, C.; Cortés, J. Distributed Safe Navigation of Multi-Agent Systems Using Control Barrier Function-Based Controllers. *IEEE Robot. Autom. Lett.* **2024**, *9*, 6760–6767. https://doi.org/10.1109/LRA.2024.3414268.
20. Lv, X.; Peng, C.; Ma, J. Control Barrier Function-Based Collision Avoidance Guidance Strategy for Multi-Fixed-Wing UAV Pursuit–Evasion Environment. *Drones* **2024**, *8*, 415. https://doi.org/10.3390/drones8080415.
21. Rabiee, P.; Hoagg, J.B. Guaranteed-Safe MPPI Through Composite Control Barrier Functions for Efficient Sampling in Multi-Constrained Robotic Systems. In Proceedings of the 2025 IEEE 64th Conference on Decision and Control (CDC), Rio de Janeiro, Brazil, 9–12 December 2025; pp. 5515–5520. https://doi.org/10.1109/CDC57313.2025.11312129.
22. Peng, Z.; Wang, J.; Wang, D.; Han, Q.L. An Overview of Recent Advances in Coordinated Control of Multiple Autonomous Surface Vehicles. *IEEE Trans. Ind. Inform.* **2021**, *17*, 732–745. https://doi.org/10.1109/TII.2020.3004343.
23. Ning, J.; Li, T.; Chen, C.L.P. Neuro-adaptive distributed formation tracking control of under-actuated unmanned surface vehicles with input quantization. *Ocean Eng.* **2022**, *265*, 112492. https://doi.org/10.1016/j.oceaneng.2022.112492.
24. Feng, G.C.; Hao, P.W.; Guo, H.N.; Li, J.W. Event-Triggered Simultaneous Tracking Control and Stabilization of Underactuated USVs. *Ocean Eng.* **2024**, *302*, 117680. https://doi.org/10.1016/j.oceaneng.2024.117680.
25. Zhu, Y.; Li, Z.; Li, Y.; Yuan, C.; Guo, G. Multi-target tracking and surrounding control for multi-USV system under unknown disturbances based on distributed NMPC. *Ocean Eng.* **2025**, *338*, 121972. https://doi.org/10.1016/j.oceaneng.2025.121972.
26. Jiang, Y.; Peng, Z.; Liu, L.; Wang, D.; Zhang, F. Safety-Critical Cooperative Target Enclosing Control of Autonomous Surface Vehicles Based on Finite-Time Fuzzy Predictors and Input-to-State Safe High-Order Control Barrier Functions. *IEEE Trans. Fuzzy Syst.* **2024**, *32*, 816–830. https://doi.org/10.1109/TFUZZ.2023.3309706.
27. Li, R.; Gu, N.; Wang, D.; Peng, Z.; Zhang, W. Safety-Critical Cooperative Pursuit Planning and Control of Multiple Autonomous Surface Vehicles Against a Partially Unknown Faster Evader. *IEEE Trans. Control Netw. Syst.* **2026**, *13*, 487–496. https://doi.org/10.1109/TCNS.2025.3649094.
28. Kennedy, J.; Eberhart, R. Particle Swarm Optimization. In Proceedings of the ICNN'95—International Conference on Neural Networks, Perth, WA, Australia, 27 November–1 December 1995; Volume 4, pp. 1942–1948. https://doi.org/10.1109/ICNN.1995.488968.
29. Fossen, T.I. *Handbook of Marine Craft Hydrodynamics and Motion Control*, 2nd ed.; Wiley: Hoboken, NJ, USA, 2021. https://doi.org/10.1002/9781119575016.
30. Guo, B.Z.; Zhao, Z.L. On the convergence of an extended state observer for nonlinear systems with uncertainty. *Syst. Control Lett.* **2011**, *60*, 420–430. https://doi.org/10.1016/j.sysconle.2011.03.008.

Disclaimer/Publisher's Note: The statements, opinions and data contained in all publications are solely those of the individual author(s) and contributor(s) and not of MDPI and/or the editor(s). MDPI and/or the editor(s) disclaim responsibility for any injury to people or property resulting from any ideas, methods, instructions or products referred to in the content.